THE UNIQUE CYTOARCHITECTURE AND WIRING OF THE HUMAN DEFAULT MODE NETWORK

Casey Paquola[1,2], Margaret Garber[1], Stefan Frässle[3], Jessica Royer[1], Shahin Tavakol[1], Raul Rodriguez-Cruces[1], Donna Gift Cabalo[1], Sofie Valk[2,4], Simon Eickhoff[2], Daniel S. Margulies[5], Alan Evans[1], Katrin Amunts[6], Elizabeth Jefferies[7], Jonathan Smallwood[8*], Boris C. Bernhardt[1*]

[1]*McConnell Brain Imaging Centre, Montreal Neurological Institute, McGill University, Montréal, Quebec, Canada*

[2]*Institute for Neuroscience and Medicine, INM-7, Forschungszentrum Jülich, Jülich, Germany*

[3]*Translational Neuromodeling Unit (TNU), University of Zurich & ETH Zurich, Zurich, Switzerland*

[4]*Max Planck Institute for Cognitive and Brain Sciences, Leipzig, Germany*

[5]*Integrative Neuroscience & Cognition Center (INCC – UMR 8002), University of Paris, Centre national de la recherche scientifique (CNRS)*

[6]*Institute for Neuroscience and Medicine, INM-1, Forschungszentrum Jülich, Jülich, Germany*

[7]*Department of Psychology, University of York, York, United Kingdom*

[8]*Department of Psychology, Queen's University, Kingston, Ontario, Canada*

[*]Equal contribution

SUMMARY

The default mode network (DMN), a set of brain regions in parietal, temporal and frontal cortex, is implicated in many aspects of complex thought and behavior. However, understanding the role of the DMN is complicated because is implicated in functional states that bridge traditional psychological categories and that may have antagonistic features, notably perceptually-decoupled mind-wandering *vs* perceptually-driven decision making. Here, we leverage *post mortem* histology and high field *in vivo* neuroimaging to show how the anatomy of the DMN helps to explain its broad functional associations. The DMN contains cytoarchitecture associated with unimodal, heteromodal, and memory-related processing, an architecture that can enable complex behaviours dependent on integration of perception and memory. Anatomically, the DMN contains regions receptive to input from sensory cortex and a core that is relatively insulated from environmental input, a division that may explain the network's role in internally- and externally-focussed states. Finally, the DMN is unique amongst cortical networks in balancing its output across the levels of sensory processing hierarchies, a pattern that may help coordinate and homogenise distributed neural function. Together, our study establishes an anatomical foundation for mechanistic accounts of how the DMN contributes to human thought and behaviour by integrating experiences of the inner and outer worlds.

MAIN

The default mode network (DMN) is a distributed set of brain regions in the frontal, temporal, and parietal lobes with strongly correlated fluctuations in function[1–3]. It is among the most important, yet challenging discoveries of modern neuroscience[4,5]. This network is notable for its associations with distinctively human features of cognition, including our sense of self[6], declarative memory[7], daydreaming[8,9], creativity[10], conceptual combinations[11], social cognition[12], and it is at the core of prominent theories of psychiatric[13] and neurological illness[14]. Theories on the role of the DMN initially focused on internally-oriented cognition and its antagonism with "task-positive" networks[15,16], but increasing evidence shows DMN activity is related to the content of external stimuli[17,18] as well as externally-oriented task demands[9,11,19], and DMN subregions can co-fluctuate with regions of "task-positive" networks[20–22]. Thus, the conceptual challenge posed by the DMN is understanding how a neural system can be involved in so many different states, particularly since many are seemingly antagonistic, such as perceptually-driven decision making[23] and perceptually-decoupled mind-wandering[24–26].

Recent perspectives have argued that resolving the role of the DMN in cognition depends on understanding its anatomy[16,27,28]. At a macroscale, DMN regions are maximally distant from primary sensory and motor areas[29]. This topography may allow neural activity in the DMN to be decoupled from perception of the here and now[27], as neural signals are incrementally transformed across cortical areas from those capturing details of sensory input towards more abstract features of the environment[30,31]. These observations suggest neural activity in the DMN has the potential to be both distinct from sensory input, while also incorporating abstract representations of the external world. This, together, could explain its involvement across such diverse contexts[27]. Although this topographical perspective, in principle, accounts for its broad involvement in human cognition, we lack a detailed explanation of how the neural circuitry within the DMN enables this hypothesised role[32].

We set out to describe the microarchitecture and wiring of this system to provide a set of anatomical constraints on views of how the DMN contributes to cognition. We capitalise on a combination of quantitative *post mortem* histology and multimodal *in vivo* neuroimaging to map DMN microarchitecture, and examine how microarchitecture contributes to its structural and functional embedding in the brain. In particular, we leverage (i) an established atlas of cytoarchitectural taxonomy ("cortical types")[33,34], (ii) whole-brain 3D histology for fine-grained cytoarchitectonic mapping[35,36] and (iii) multimodal *in vivo* neuroimaging for approximations of structural wiring and functional flow. Finally, (iv) using ultrahigh-field 7 Tesla (7T) MRI, we demonstrate how the discovered relationship between microarchitecture, connectivity and function of the DMN exist within an individual.

CYTOARCHITECTURAL HETEROGENEITY

The DMN is generally agreed to encompass the (1) parahippocampal cortex, (2) precuneus and posterior cingulate cortex, (3) a caudal region of the inferior parietal lobule, (4) middle temporal

cortex, (5) inferior frontal and (6) medial prefrontal cortex[16,37,38]. Throughout our primary analyses, we use the most common atlas of the default mode network[2] (**Figure 1A**). In supplementary analyses, we show the replicability of key findings with alternative delineations of the DMN.

The most noticeable difference in cytoarchitecture across the cortex is the degree of laminar differentiation. Degree of laminar differentiation is highest in primary sensory areas and decreases along the cortical mantle in a graded manner, reaching a low in agranular cortex, which neighbours hippocampal and piriform allocortex. This gradient of laminar differentiation is synopsised by six cortical types, originally defined by Von Economo[33,34](**Figure 1A)**. Patterns of projections also systematically vary along this gradient[39–42], forming a hierarchical architecture spanning from primary sensory areas to the prefrontal cortex and hippocampus[43–45]. Notably, the cortical types (synonymous with the levels of sensory hierarchies) are hypothesised to reflect different specialisations of the underlying cortical microcircuits, ranging from externally-focused sensory areas through unimodal and heteromodal cortex to internally-focused agranular areas[46,47]. This relationship, theorised primarily on neurophysiological evidence in non-human primates and lesion studies in humans[47,48], is supported here by meta-analytical decoding of the cortical types, using activation maps from thousands of functional MRI studies (**Supplementary Figure 1**).

Based on overlap of the DMN atlas with a cytoarchitectonic atlas of cortical types[33,34], we found the DMN contains five of six cortical types (**Figure 1A**). This make-up was distinctive, relative to other functional networks (**Supplementary Table 1,** all Kolgomorov-Smirnoff tests>0.11, $p<0.001$). The DMN contains cortical types commonly associated with processing of sensory information and its progressive integration (eulaminate-I, II, and III), but it also contains dysgranular and agranular cortex that are often linked to processes such as memory[47] (**Supplementary Figure 1**). These cortical types are not equally represented within the DMN, however ($\chi^2=1497$, $p<0.001$). Approximately 90% of the DMN is eulaminate. The high proportion of eulaminate may be expected given the prevalence of these types across the whole cortex (84%; **Supplementary Table 1**). To evaluate how these cortical types are represented in the DMN, we compared the proportion of cortical types within the DMN and within 10,000 rotated versions of the DMN. The rotated versions are generated by randomly spinning the functional network atlas on a spherical representation of the cortex, providing a null distribution of outcome statistics that account for the network's size and distribution. In doing so, we found that the DMN over-represents eulaminate-I (18% increase; $p_{spin}=0.006$), classically known as "heteromodal" cortex, which is hypothesised to process information from multiple sensory domains[47](**Supplementary Figure 1**). This distinctive composition of cortical types was evident regardless of slight alterations to the DMN atlas, such as defining the DMN by deactivations during tasks, task-based independent component analysis or combining individual-specific DMN annotations (**Supplement Figure 2**). The broad range of cortical types, combined with the over-representation of eulaminate-I in the

DMN, is consistent with a role of this network in integration of information from multiple systems including those linked to sensory and memory processes.

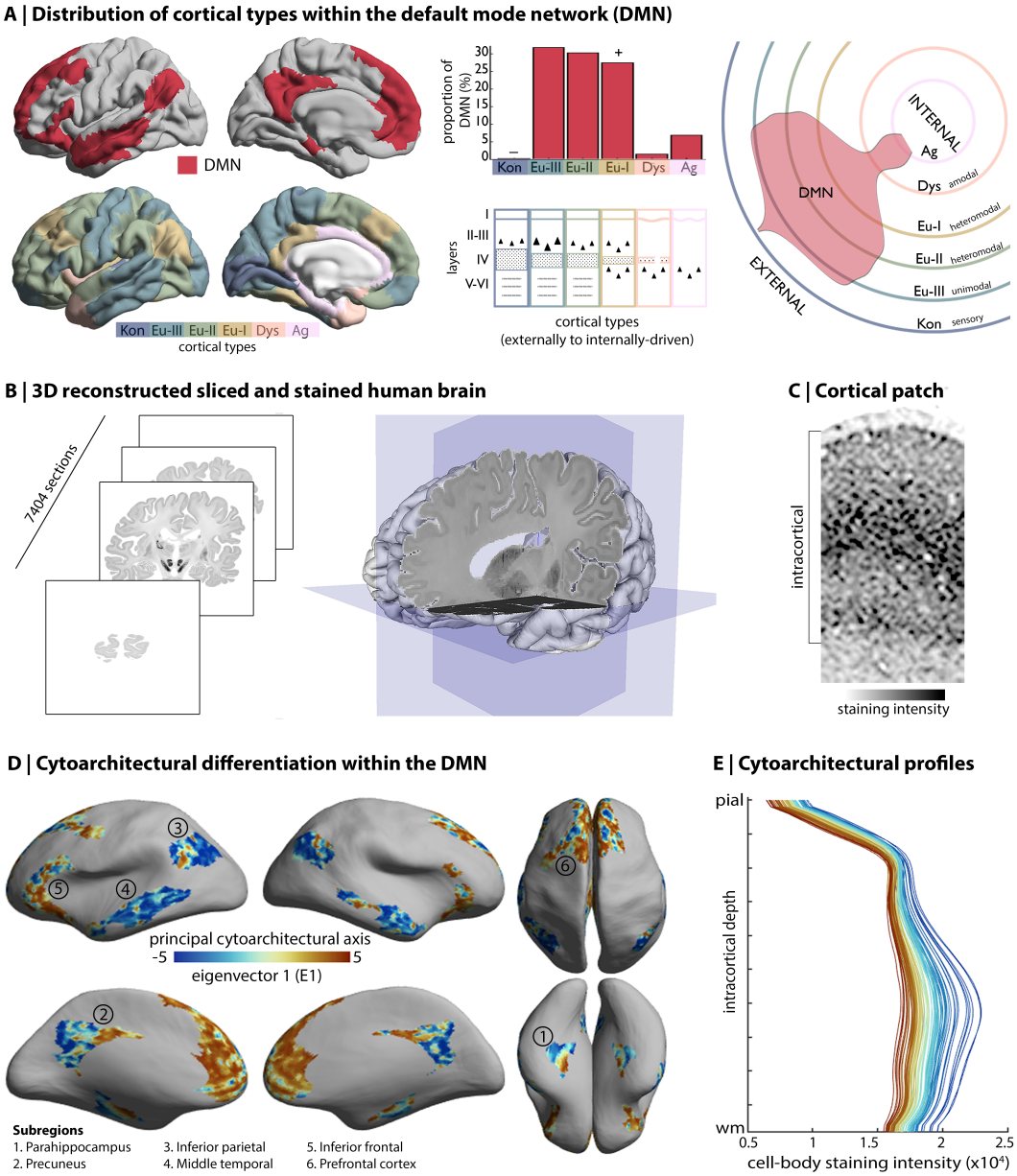

Figure 1: Cytoarchitectural heterogeneity of the DMN. A) *Upper left*. The most common atlas of the DMN, used in primary analyses and shown on the cortical surface[3]. *Lower left.* Cytoarchitectonic atlas of cortical types[33,34]. *Upper middle.* Histogram depicts the frequency of cortical types within the DMN. + is indicative of significant over-representation and – is under-representation, relative to whole cortex proportions. *Lower middle.* The schematic highlights prominent features that vary across cortical types, including the location/size of largest pyramidal neurons (triangles), thickness of layer IV, existence of sublayers in V-VI (grey dashed lines), regularity of layer I/II boundary (straightness of line). Kon=koniocortical. Eul=eulaminate. Dys=dysgranular. Ag=agranular. *Right.* Circular plot represents the spread of the DMN from externally- to internally-driven cortical types. **B)** 7404 coronal slices of cell-body-stained sections (20 µm thickness) were reconstructed into a 3D human brain model, BigBrain[35]. **C)** Example cortical patch shows depth-wise variations in cell-body-staining in BigBrain. **D)** The principal eigenvector (*E1*) projected onto the inflated BigBrain surface shows the patterns of cytoarchitectural differentiation within the DMN. Subregion names are provided in F. **E)** Line plots represent cell-body-staining intensity by intracortical depth (from pial to white matter boundary) at different points along E1. Cortical points with lower E1 (*blue*) have peaked cellular density in mid-deep cortical layers, indicative of pronounced laminar differentiation, whereas cortical points with higher E1 (*red*) have more consistent cellular density across cortical layers, illustrating lower laminar differentiation. **F)** The topography of E1 in each subregion shown as 3D surface plots, with E1 as the z-axis. The x- and y-axes are defined by Isomax flattening of each subregion. Left boxplots show the proportion of variance in E1 explained by spatial axes (x,y) for each subregion and for models of increasing complexity (2nd-4th order polynomial regression). Boxplot range depicts hemisphere differences in adjusted R^2, while the centre point is the adjusted R^2 averaged across hemispheres. Right boxplots show "waviness"[49] of E1 in each subregion. Together, these metrics quantify how cytoarchitectural landscapes vary between subregions from a relatively simple gradient in the parahippocampus, well-explained by the spatial regression model and with low waviness, to marked fluctuations in the dorsal prefrontal cortex, characterised by high waviness and poor regression model performance. PHPC=parahippocampus. Prec.=precuneus. IP=inferior parietal. MT=middle temporal. IF=inferior frontal. PFC=prefrontal cortex.

Having established that the DMN contains a broad array of cortical types, we adopted data-driven approaches to characterise more fine-grained spatial patterns of cytoarchitectural variation. We transformed the functional network atlas[2] to a 3D cell-body-stained *post mortem* human brain[35] using specially tailored cortical registration procedures[36,50]. Using intracortical profiles of cell-body-staining intensity (**Figure 1C,E**), we assessed cytoarchitectural variability within the DMN. We mapped patterns of cytoarchitectural variation via unsupervised non-linear manifold learning[51] (**Figure 1D,** see also **Supplementary Figure 3**). The first eigenvector of this manifold (E1), hereafter referred to as the cytoarchitectural axis, described a shift in the shape of the underlying cytoarchitectural profiles from peaked to flat (**Figure 1E**) and reflects differences in how cellular density varies within the cortex (**Figure 1C**). The cytoarchitectural axis is anchored on one end by unimodal eulaminate-III cortex (*e.g.* retrosplenial and posterior middle temporal) and on the other by agranular cortex (*e.g.* medial parahippocampus and anterior cingulate). Thus, the endpoints of the cytoarchitectural axis are the most extreme cortical types found within the DMN (**Supplementary Figure 3**). Beyond the endpoints, however, the cytoarchitectural axis deviates from the gradient described by cortical types[33,47,52](**Supplementary Figure 3**), nor does it discriminate between subregions of the DMN, nor does it follow an anterior-posterior gradient as seen in neuronal density[53]. Instead, we observed a mosaic of different spatial topographies across DMN subregions, where neighbouring microcircuits are sometimes distinct and distant microcircuits are sometimes similar. Our data-driven approach, thus, indicates that the

organisation within the DMN is unlike those across sensory hierarchies and is less constrained by large-scale spatial gradients[54,55].

Looking closer at the topography of cytoarchitecture highlights the (dis)similarity of neighbouring microcircuits within the DMN. Given the ubiquity of connectivity between neighbouring microcircuits in the cortex[56], topography provides important information on the form of communication within spatially-contiguous subregions. Subregions of the DMN evidently vary in terms of their cytoarchitectural topography (**Figure 1F**), and we quantified these differences using two complementary measures: smoothness and waviness. We captured the smoothness of the microarchitectural landscape by evaluating the proportion of variance in the cytoarchitectural axis that could be accounted for by spatial axes and the waviness by measuring deviations from the mean, a common technique in mechanical engineering[57]. We found that subregions significantly differ in terms of both smoothness and waviness (smoothness: $2^{nd}/3^{rd}/4^{th}$ order; $F=14.5/14.9/20.1$, $p<0.004$; waviness: $F=20.6$, $p=0.001$). Smoothness was particularly high in the parahippocampus, showing that its cytoarchitectural axis follows a relatively smooth gradient here, as may be predicted from previous anatomical research[58,59]. Conversely, the prefrontal cortex exhibits especially high waviness, which aligns with classic observations in the tract-tracing literature in non-human animals and recent functional connectivity studies showing "interdigitated" connectivity patterns within this region[60–62]. This analysis establishes that the DMN contains distinct cytoarchitectural patterns representative of different hypothesised ways that neural signals can be integrated in the cortex: The mesiotemporal gradient has been associated with progressive convergence of information[63,64], whereas prefrontal interdigitation is thought to support linking information from disparate sources[60].

RECEIVERS ON THE PERIPHERY AND AN INSULATED CORE

Thus far, our analyses provided evidence that the DMN contains highly variable types and arrangements of microcircuits, which is consistent with the hypothesis that a wide range of neural signals can be integrated within the regions that make up this network. Next, we explored how the anatomical features of the DMN relate to its connectivity and whether this can explain its involvement in both perceptually-coupled and -decoupled states[23–26]. We hypothesised that connectivity would co-vary with the cytoarchitectural axis (E1, **Figure 1D**), because propensity for connectivity increases with cytoarchitectural similarity[40,65,66]. Nevertheless, this principle is based on sensory hierarchies[45,47,67], and it so far remained unclear whether, and how, it would generalise to the DMN.

First, we measured communication efficiency along white matter tracts[68] using high-field diffusion magnetic resonance imaging (MRI) tractography . We found that the propensity to communicate with other cortical areas (indexed by average "navigation efficiency", see *Methods* for details) varied within the DMN [coefficient of variation (CoV)=18%]. Navigation efficiency with the rest of the cortex was significantly higher towards one end of the DMN's cytoarchitectural axis,

specifically those areas of the DMN with more peaked cytoarchitectural profiles (r=-0.60, p_{spin}=0.001, **Figure 2Ai**). This effect was particularly pronounced for communication with perceptually-coupled cortical types (koniocortical/eulaminate-III/eulaminate-II; r=-0.64/-0.60/-0.30, p_{spin}<0.025, **Figure 2Ai**). Thus, the organisation of the DMN, revealed by cytoarchitectural analysis, also reflects a constraint on communication supported by white matter tracts, especially for communication between the DMN and cortical areas engaged in sensory and unimodal processing.

Next, we examined the consequences of this structural organisation on the flow of information in the cortex. We applied a generative model of effective connectivity[70] to resting state fMRI timeseries of 400 isocortical parcels[71], then selected DMN parcels as targets for functional input analyses and DMN parcels as seeds for functional output analyses. Functionally-estimated input and output varied within the DMN (CoV=24% and 29%, respectively). Average strength of input was significantly higher to those areas of the DMN with more peaked cytoarchitectural profiles (r=-0.41, p_{spin}<0.001), in line with the structural analysis. Examination of type-specific connectivity showed limited discrimination between cortical types, whereby inputs from externally- and internally-focused cortical types were all concentrated on DMN areas with peaked cytoarchitectural profiles (**Figure 2Aii-iii, Supplementary Table 2**). Thus, multiple inputs converge upon a subset of DMN subunits, while a subset of DMN subunits, those with flat cytoarchitectural profiles, remained relatively insulated from cortical input. Output did not co-vary with the cytoarchitectural axis (r=-0.05, p_{spin}=0.069, **Figure 2Aii-iii**). These findings were consistent in a replication dataset and when including subcortical structures and the hippocampus in the model (**Supplementary Table 2**). Together, these analyses suggest the DMN comprises two microarchitecturally distinct subsets - one with highly efficient tract-based communication with cortical areas implicated in perception and action while receiving convergent input from across all levels of sensory hierarchies, and another that exhibits less efficient tract-based communication with the rest of the cortex and is relatively insulated from input signals from sensory systems (**Figure 2B**).

A UNIQUE BALANCE OF OUTPUT

Focusing on the anatomy of the DMN revealed its distinctive pattern of cytoarchitectural heterogeneity, which constrains how it communicates with other systems. Now, we turn our attention to how these anatomical properties contribute to the unique position of the DMN in the large-scale functional organisation of the cortex by understanding how extrinsic connectivity of the DMN is distributed across cortical types.

First, we discovered that the DMN communicates in a balanced manner with all cortical types. Compared to all other functional networks, the DMN exhibits the most balanced efficiency of communication across cortical types (*i.e.,* lowest KL divergence from null model, **Supplementary Figure 4**, see **Supplementary Table 3** for full statistics). Importantly, using our functional model,

we could specify that output of the DMN is balanced across the cortical types, but input is not (**Figure 2Ci**, see **Supplementary Table 3** for full statistics and replication). In other words, the DMN outputs signals in approximately equal strength to all types of cortex (*i.e.* all levels of sensory hierarchies). Of all the functional systems in the human cortex, only the DMN exhibited this balance in output across cortical types (**Figure 2Cii**). The spatial distribution, internal heterogeneity and connectivity of the DMN, thus, engender a unique ability to receive temporally distinct signals and then send neural signals that influence all levels of the sensory hierarchies in a similar manner.

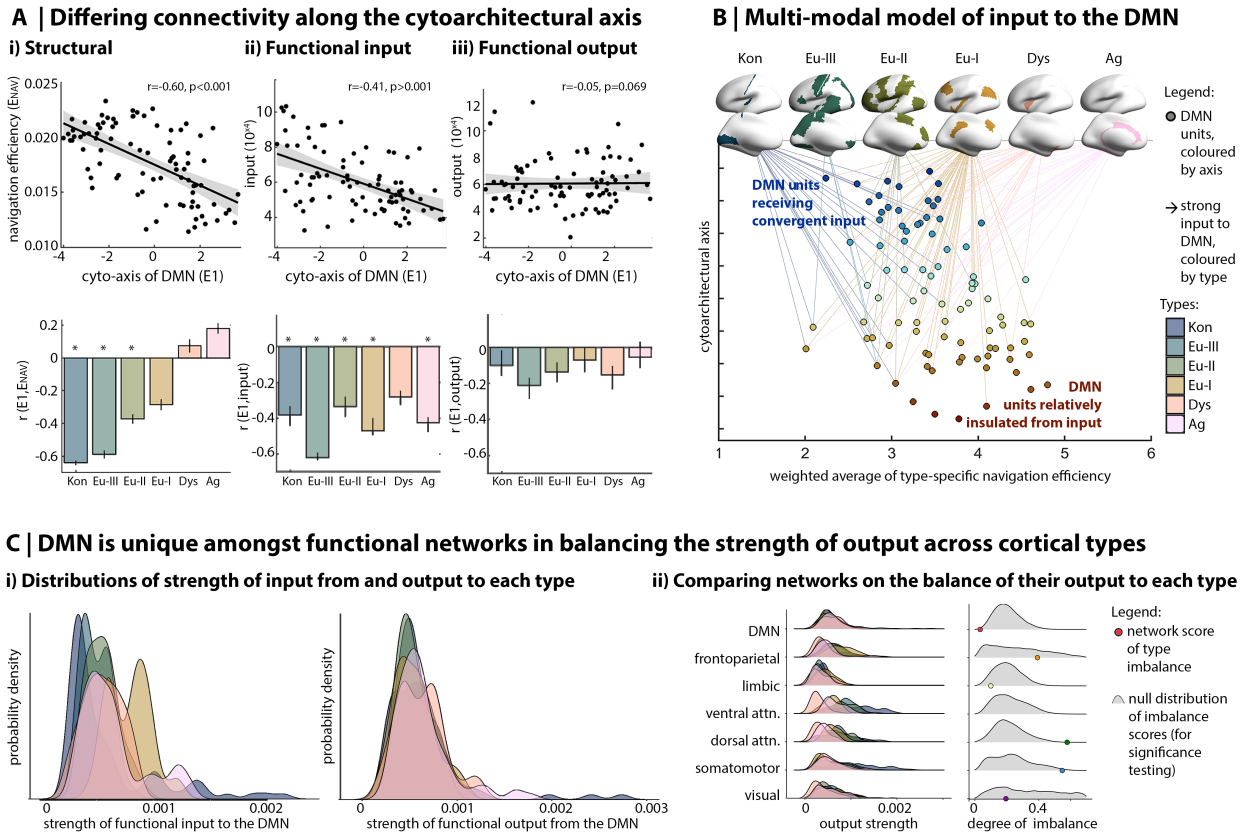

Figure 2: Organisation of DMN connectivity. A) *Above.* Scatterplots show the correlation of the cytoarchitectural axis (E1) with average extrinsic (i) structurally-modelled navigation efficiency, (ii) functionally-modelled input and (iii) functionally-modelled output. *Below.* Bar plots shows the linear correlation coefficient (r) of E1 with average connectivity to each cortical type. The stability of the correlation coefficient was calculated by repeating the procedure in 10 folds, each including 90% of datapoints. Error bars indicate the standard deviation of the r value across folds. Significant (*) negative r values indicate that DMN nodes with peaked profiles have (i) higher navigation efficiency with externally-focused cortical types, and (ii) stronger input from most cortical types. Kon=koniocortical. Eul=eulaminate. Dys=dysgranular. Ag=agranular. **B)** Multi-modal model of DMN organisation shows the dual character of the DMN, including areas with convergent input and insulated areas. All points in the scatterplot represent units of the DMN, are coloured by position along the cytoarchitectural axis (also y-axis) and are organised along the x-axis based on weighted average of type-specific navigation efficiency. Top 75% of functionally-defined inputs are shown. **C)** (i) Coloured ridge plots show probability distributions of connectivity between the DMN and each cortical type. Notably, for functional output the DMN exhibits overlapping, normal distributions, whereas for functional type-wise differences are evident. **ii.** Focusing on functional output, coloured ridge plots show distributions for all networks, illustrate more balance between types in the DMN. *Right.* The imbalance of connectivity to distinct cortical types was evaluated as the Kullback-Leibler (KL) divergence from a null model with equal connectivity to each type. The coloured dots show the empirical KL divergence for each network and the grey density plots show the null distribution

of KL divergence values based on 10,000 spin permutations. Permutation testing indicated that the DMN is unique, among functional networks in balancing output across cortical types.

CORRESPONDENCE OF MICROARCHITECTURE AND CONNECTIVITY WITHIN AN INDIVIDUAL

To demonstrate that our findings generalise to single individuals, we acquired high-resolution quantitative T1 (qT1) relaxometry MRI, alongside diffusion weighted and functional MRI in eight healthy individuals using an ultrahigh-field 7 Tesla MRI system. Methods were identical to those described above, except that histology was replaced by qT1. We hypothesised that qT1, sensitive to cortical myelin, could recapitulate regional differences in cytoarchitecture, because cortical areas and intracortical layers defined on cyto- or myelo-architecture align[72,73], and our previous work has shown strong correspondence of principal axes of microstructural differentiation derived from histology and qT1 MRI[52]. While the qT1 and histological datasets differ in terms of biological sensitivity (myelin *vs* cell bodies) and resolution (500µm *vs* 100µm), the patterns of microarchitectural differentiation in the DMN significantly overlapped between the modalities (r_{avg}=0.32, p_{avg}<0.001), for example highlighting microstructural differences of the prefrontal cortex from the lateral temporal region (**Figure 3A**). Notably, the topography of microarchitectural differentiation was similar in both qT1 and histological datasets, varying from a smooth gradient in the mesiotemporal lobe to higher waviness in the prefrontal cortex (**Figure 3B**). Indeed, subregion smoothness (r_{avg}=0.51, p_{avg}=0.09) and waviness (r_{avg}=0.90, p_{avg}<0.001) were strongly correlated between the datasets.

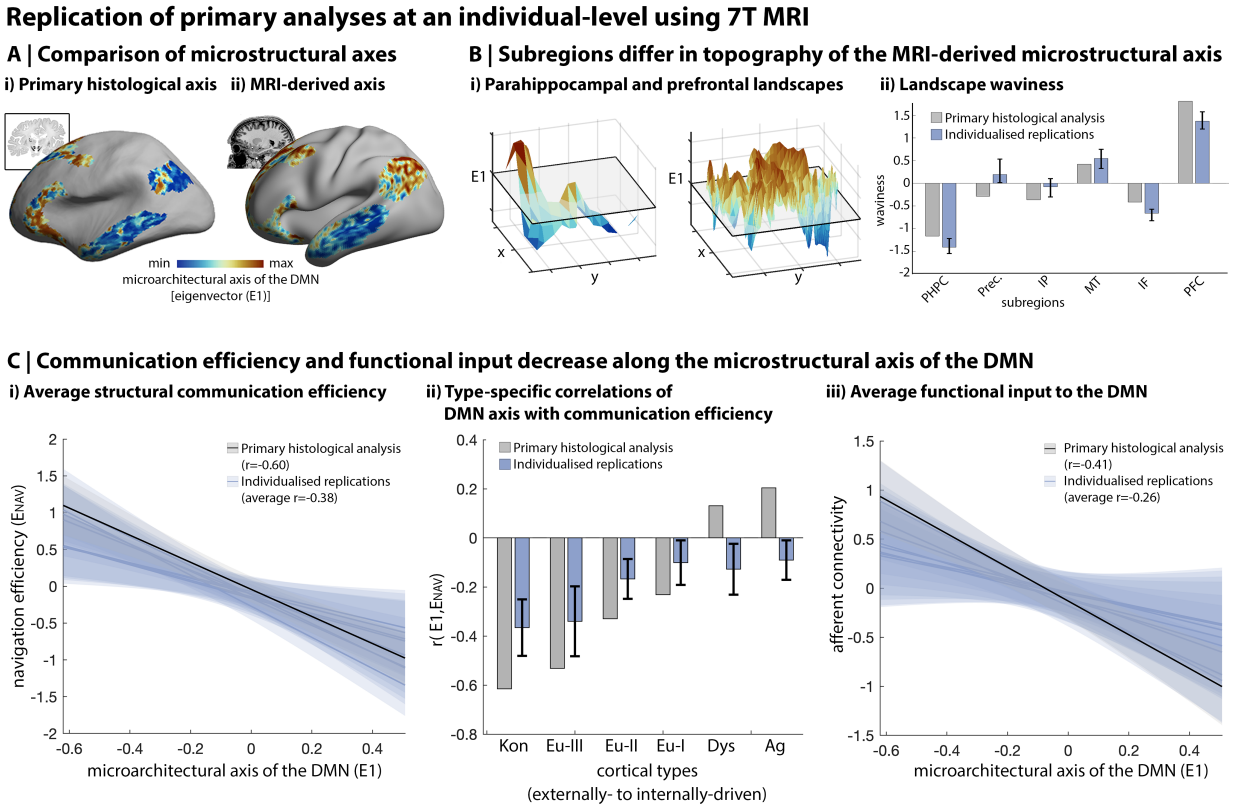

Figure 3: A) (i) The principal eigenvector of microstructural variation in the DMN (E1) was extracted from myelin-sensitive quantitative MRI (qT1)[74], in line with the procedure employed on the histological dataset ("BigBrain"), revealing strikingly similar patterns. **B)** The roughness of MRI-derived microstructural differentiation varied between subregions in line with histological evidence. The parahippocampus exhibited a graded transition from high-to-low E1, reflected by high smoothness and low waviness, whereas the prefrontal cortex exhibited an undulating landscape with high waviness. **C)** Using individual-specific measures, we consistently found that cortical points with higher E1 were associated with *(left)* lower average navigation efficiency, (*centre*) especially lower navigation efficiency with perceptually-coupled cortical types, and (*right*) lower functional input. Thus, in line with histological evidence, the MRI-based approach highlights that a subsection of the DMN is relatively insulated from external input. Line plots are presented with 95% confidence interval shading.

In line with the primary analyses, we also observed a higher communication efficiency between DMN subregions and the rest of the cortex towards one end of the microstructural axis (r_{avg}=-0.38, $p_{avg\text{-}spin}$=0.015), and this effect was especially pronounced with regards to communication to perceptually-coupled cortical types (koniocortical/eulaminate-III: r_{avg}=-0.40/0.37, $p_{avg\text{-}spin}$=0.044/0.089). Functional input also tended to decrease along the microstructural axes (r_{avg}=-0.26, $p_{avg\text{-}spin}$=0.101). Together, these individual-level analyses reinforce the notion that the microarchitectural axis of the DMN discriminates a zone of multi-modal convergence from a core that is relatively insulated from external input (**Figure 3C**).

DISCUSSION

Historically, anatomical details of brain systems have helped to constrain accounts of their function[45,75]. Our study extended this perspective to the human default mode network (DMN), one of the most extensively studied yet least well understood systems. Leveraging *post mortem* histology and ultrahigh field *in vivo* MRI, we provide a novel account of how the "hardware" of the DMN can theoretically allow it to contribute to a broad range of cognitive states[16,27,38,38]. Indeed, we observed that the DMN contains diverse microcircuits that are specialised for modality-specific, transmodal, and self-generated processing[33,47,76]. This versatility is important because it enables direct exchange of the DMN with both sensory systems interacting with the outside world and self-generated memory processes[67]. In addition, we observed that the DMN contains regions that receive input from multiple other cortical regions and a core that is relatively insulated from input. The associations between external and internal modes of cognition and the DMN may thus be explained by shifting the functional balance from input-oriented to more insulated regions. Such a mechanism would also align with functional imaging studies showing regional differentiation within the DMN for different tasks[38,77], such as reading vs. mind-wandering[78].

Neuroanatomical insights provide a foundation of how the DMN architecture shapes aspects of cognition. For instance, the topography of cytoarchitecture sheds light on the different forms of information integration, because more than 90% of cortico-cortical connections are between neighbouring microcircuits[56]. We observed microarchitectural gradients in the mesiotemporal subregion, a pattern previously linked to sequential transformation of signals from low- to higher-order representations[29,79] and a gradual shift in functional connectivity from the "multiple demand"

network to fronto-temporal pole areas[58,80]. In contrast, the interwoven layout of different microcircuits within prefrontal subregions, related to interdigitation[60,61], may provide a structural substrate to support domain specialisation[62,81,82] and cross-domain integration[60]. The unique presence of both graded and interdigitated motifs within the DMN suggests that when these regions function as a collective, they could theoretically contribute to whole brain function in a manner that combines two different types of integration. As our replication analysis using ultrahigh-field MRI systems has shown, these fine-grained insights into microarchitecture, connectivity, and function persist at an individual-level and *in vivo.* In other words, they can be seen using microstructural and functional data in a single subject and not just based on population level imaging data or singular *post mortem* resources such as the one studied here. Extending these methods to *in vivo* imaging also opens unprecedented possibilities to interrogate how microarchitecture and its inter-individual variation manifest in cognition and behaviour in future studies.

Our investigation of DMN microarchitecture can help to discern the network's relationship to cortical hierarchies. Established by foundational research in non-human animals and increasingly confirmed in the human brain, hierarchies are a recurring motif in cortical organisation[42,43]. Hierarchical architectures are related to inter-regional variations in temporal dynamics[83,84] and neural representations, in particular the construction of abstract neural codes in regions of association cortex[30,47]. Sensory hierarchies are well-documented in the neuroscientific literature[45], and their properties can be confirmed directly through the stimulation of sensory systems. However, hierarchies in association networks are more challenging to determine[55], in part due to the lack of a ground truth of their 'bottom' and 'top'. In lieu of such functional evidence, our microarchitectural findings are invaluable, as they show that the DMN entails two properties of hierarchies, namely connectivity organisable by distinct levels as well as the existence of an apex that is relatively insulated from external input. Unlike sensory hierarchies, however, which increasingly intersect at upper levels, the internal organisation of the DMN is less constrained by spatial gradients and exhibits more balanced interfacing with multiple levels of sensory systems as well as the limbic system. One may speculate that this unique architecture helps to unify neural activity across brain systems or verify predictions of the world against memory in real time[27,85]. By expanding the conceptualisation of hierarchies beyond sensory systems, we hope to illuminate the diverse nature of information processing in the brain, which is critical to understanding the implementation of human cognition.

In sum, this work provided a novel account on the DMN's unique architecture that consolidates seemingly disparate principles of neuroanatomy, showing how hierarchical and parallel processing co-exist and interact in the human brain. In this way, our study offers a potential solution to how the architecture of the human brain may enable the formation of abstract representations and uses these to inform cognition across a range of domains. Specifically, the functional multiplicity of the DMN is pillared upon its internal heterogeneity, possession of receivers and more insulated

subunits as well as its balanced communication with all levels of sensory hierarchies. Together, this set of unique features outlines an anatomical landscape within the DMN that may explain why the DMN is involved in states that cross traditional psychological categories and that can have opposing features. In the future, this architecture may provide a foundation to understand how the DMN contributes to uniquely human capacities such as intelligence, memory, as well as conscious experience.

METHODS

Histological data

An ultra-high resolution 3D reconstruction of a sliced and cell-body-stained *post mortem* human brain from a 65-year-old male was obtained from the open-access BigBrain repository on September 1, 2020 [https://bigbrain.loris.ca/main.php;[35]]. The *post mortem* brain was paraffin-embedded, coronally sliced into 7,400 20µm sections, silver-stained for cell bodies[86] and digitised. Manual inspection for artefacts (*i.e.,* rips, tears, shears, and stain crystallisation) was followed by automatic repair procedures, involving non-linear alignment to a *post mortem* MRI of the same individual acquired prior to sectioning, together with intensity normalisation and block averaging[87]. The 3D reconstruction was implemented with a successive coarse-to-fine hierarchical procedure[88]. We downloaded the 3D volume at 100µm resolution, which was the highest resolution available for the whole brain. Computations were performed on inverted images, where intensity reflects greater cellular density and soma size. Geometric meshes approximating the outer and inner cortical interface (*i.e.,* the GM/CSF boundary and the GM/WM boundary) with 163,842 matched vertices per hemisphere were also obtained[89].

We constructed 50 equivolumetric surfaces between the outer and inner cortical surfaces . The equivolumetric model compensates for cortical folding by varying the Euclidean distance, ρ, between pairs of intracortical surfaces throughout the cortex to preserve the fractional volume between surfaces[91]. ρ was calculated as follows for each surface

$$\rho = \frac{1}{A_{out} - A_{in}} \cdot \left(-A_{in} + \sqrt{\alpha A_{out}^2 + (1 - \alpha) A_{in}^2} \right) \quad (1)$$

where α represents fraction of the total volume of the segment accounted for by the surface, while A_{out} and A_{in} represent the surface area of the outer and inner cortical surfaces, respectively. Vertex-wise staining intensity profiles were generated by sampling cell-staining intensities along linked vertices from the outer to the inner surface. Smoothing was employed in tangential and axial directions to ameliorate the effects of artefacts, blood vessels, and individual neuronal arrangement. The tangential smoothing across depths was enacted for each staining profile independently, using an iterative piece-wise linear procedure that minimises shrinkage [3 iterations[92]]. Axial surface-wise smoothing was performed at each depth independently and involved moving a 2-vertex FWHM Gaussian kernel across the surface mesh using SurfStat[93]. The staining intensity profiles are made available in the BigBrainWarp toolbox[36].

Comparison of cortical atlases

Functional networks were defined using a widely used atlas[2]. The atlas reflects clustering of cortical vertices according to similarity in resting state functional connectivity profiles, acquired in 1000 healthy young adults. Cortical types were assigned to Von Economo areas[34,94], based on a recent re-analysis of Von Economo micrographs[33]. Several features were used to identify the type, including "development of layer IV, prominence (denser cellularity and larger neurons) of deep (V–VI) or superficial (II–III) layers, definition of sublayers (*e.g.,* IIIa and IIIb), sharpness of boundaries between layers, and presence of large pyramids in superficial layers" [33]. Cortical types synopsise degree of granularity, from high laminar elaboration in koniocortical areas, six identifiable layers in eulaminate III-I, poorly differentiated layers in dysgranular and absent layers in agranular.

The proportion of DMN vertices assigned to each cortical type was calculated on a common surface template, fsaverage5[95]. The equivalence of cortical type proportions in the DMN and each other functional network was evaluated via pair-wise Kolgomorov-Smirnoff tests. Significant over- or under-representation of each cortical type within the DMN was evaluated with spin permutation testing[96]. Spin permutation testing, used throughout following statistical analyses, involves generating a null distribution by rotating one brain map 10,000 times and recomputing the outcome of interest. Then, we calculate $p_{spin} = 1 - \frac{\Sigma\,(empirical > permutations)}{total\ permutations}$ and/or $p_{spin} = 1 - \frac{\Sigma\,(empirical < permutations)}{total\ permutations}$[97]. The null distribution preserves the spatial structure of both brain maps, which establishes the plausibility of a random alignment of the maps explaining their statistical correspondence. Generally, we deemed significance $p<0.05$ for one-tailed tests and $p<0.025$ for two-tailed tests. Additionally, we used Bonferroni correction when multiple univariate comparisons were made using the same response variable. In the case of the over- or under-representation of specific cortical types within the DMN, we randomly rotated the cortical type atlas, then generated null distributions, representing the number of vertices within the DMN assigned to each type.

The robustness of cytoarchitectural heterogeneity to the DMN definition was assessed with three alternative atlases. Given the origins of the DMN as a "task-negative" set of regions[4,5], the first alternative atlas involved identifying regions that are consistently deactivated during externally-oriented tasks. In line with a recent review[27], we used pre-defined contrast maps from 787 healthy young adults of the Human Connectome Project ("HCP_S900_GroupAvg_v1 Dataset"). Each map represents the contrast between BOLD response during a task and at baseline. Fifteen tasks were selected to correspond to early studies of the DMN[5] [Working Memory (WM)–2 Back, WM-0 Back, WM-Body, WM-Face, WM-Place, WM-Tool, Gambling-Punish, Gambling-Reward, Motor-Average, Social-Random, Social-Theory of Mind, Relational-Match, Relational-Relation, Emotion-Faces, Emotion-Shapes]. For each contrast, task-related deactivation was classed as z-score≤-5, which is consistent with contemporary statistical thresholds used in neuroimaging to

reduce false positives[98]. The second alternative atlas represented an independent component analysis of 7,342 task fMRI contrasts. The DMN was specified as the fourth component. The volumetric z-statistic map for that component was projected to the cortical surface for analysis. Thirdly, A probabilistic atlas of the DMN was calculated as the percentage of contrasts with task-related deactivation. The second alternative atlas represented the probability of the DMN at each vertex, calculated across 1029 individual-specific functional network delineations[99]. For each alternative atlas, we calculated the proportions of cortical types across a range of probabilistic thresholds (5-95%, at 5% increments) to determine whether the discovered cytoarchitectural heterogeneity of the DMN was robust to atlas definition.

Data-driven cytoarchitectural axis within the DMN

The functional network atlas was transformed to the BigBrain surface using a specially optimised multimodal surface matching algorithm[36,50]. The pattern of cytoarchitectural heterogeneity in the DMN was revealed using non-linear manifold learning. The approach involved calculating pair-wise product-moment correlations of BigBrain staining intensity profiles, controlling for the average staining intensity profile within the DMN. Negative values were zeroed to emphasise the non-shared similarities. Diffusion map embedding of the correlation matrix was employed to gain a low dimensional representation of cytoarchitectural patterns[51,96]. Diffusion map embedding belongs to the family of graph Laplacians, which involve constructing a reversible Markov chain on an affinity matrix. Compared to other nonlinear manifold learning techniques, the algorithm is relatively robust to noise and computationally inexpensive[100,101]. A single parameter α controls the influence of the sampling density on the manifold ($\alpha = 0$, maximal influence; $\alpha = 1$, no influence). As in previous studies[29,52,96], we set $\alpha = 0.5$, a choice retaining the global relations between data points in the embedded space. Notably, different alpha parameters had little to no impact on the first eigenvector (spatial correlation of eigenvectors, $r>0.99$).

The DMN comprised 71,576 vertices on the BigBrain surface, each associated with approximately $1mm^2$ of surface area. Pair-wise correlation and manifold learning on 71,576 data points was computationally infeasible, however. Thus, we performed a 6-fold mesh decimation on the BigBrain surface to select a subset of vertices that preserve the overall shape of the mesh. Then, we assigned each non-selected vertex to the nearest maintained vertex, determined by shortest path on the mesh (ties were solved by shortest Euclidean distance). Staining intensity profiles were averaged within each surface patch of the DMN, then the dimensionality reduction procedure was employed. Subsequent analyses focused on the first eigenvector (E1), which explained the most variance in the affinity matrix (approximately 28% of variance). Additionally, we repeated this analysis with a highly conservative delineation of the DMN (generated by using the intersection of the three abovementioned alternative atlases), thereby demonstrating that slight variations in atlas definition do not impact the organisation of cytoarchitecture that we discovered in the network.

Local variations in E1 were examined within spatially contiguous regions of the DMN. Quantitative description of E1 topography within each subregion was achieved with two complementary approaches. First, to characterise the smoothness and complexity of the landscape, we fit polynomial models between E1 and two spatial axes[102]. The spatial axes were derived from an Isomax flattening of each subregion, resulting in a 2D description of each subregion. We compared adjusted R^2 between subregions within each polynomial order (quadratic, cubic and quartic) using a one-way ANOVA, whereby each subregion was represented by a left and right hemisphere observation. Second, to characterise the bumpiness of subregion landscapes, we adopted an approach from material engineering for characterising the roughness of a surface[49,57]. Specifically, we calculated "waviness", the ratio of the number of vertices in the subregion by absolute average deviation of E1 from the mean. As above, we compared waviness between subregions using a one-way ANOVA.

MRI acquisition and processing – Primary analyses

Primary MRI analyses were conducted on 40 healthy adults from the microstructure informed connectomics (MICs) cohort (14 females, mean±SD age=30.4±6.7, 2 left-handed)[103]. Scans were completed at the Brain Imaging Centre of the Montreal Neurological Institute and Hospital on a 3T Siemens Magnetom Prisma-Fit equipped with a 64-channel head coil. Two T1w scans with identical parameters were acquired with a 3D-MPRAGE sequence (0.8mm isotropic voxels, TR=2300ms, TE=3.14ms, TI=900ms, flip angle=9°, iPAT=2, matrix=320×320, 224 sagittal slices, partial Fourier=6/8). T1w scans were visually inspected to ensure minimal head motion before they were submitted to further processing. A spin-echo echo-planar imaging sequence with multi-band acceleration was used to obtain DWI data, consisting of three shells with b-values 300, 700, and 2000s/mm^2 and 10, 40, and 90 diffusion weighting directions per shell, respectively (1.6mm isotropic voxels, TR=3500ms, TE=64.40ms, flip angle=90°, refocusing flip angle=180°, FOV=224×224 mm^2, slice thickness=1.6mm, multiband factor=3, echo spacing=0.76ms, number of b0 images=3). One 7 min rs-fMRI scan was acquired using multiband accelerated 2D-BOLD echo-planar imaging (3mm isotropic voxels, TR=600ms, TE=30ms, flip angle=52°, FOV=240×240mm^2, slice thickness=3mm, multiband factor=6, echo spacing=0.54ms). Participants were instructed to keep their eyes open, look at a fixation cross, and not fall asleep. Two spin-echo images with reverse phase encoding were also acquired for distortion correction of the rs-fMRI scans (phase encoding=AP/PA, 3mm isotropic voxels, FOV=240×240mm^2, slice thickness=3mm, TR=4029 ms, TE=48ms, flip angle=90°, echo spacing=0.54 ms, bandwidth= 2084 Hz/Px).

An open access tool was used for multimodal data processing[104]. Each T1w scan was deobliqued and reoriented. Both scans were then linearly co-registered and averaged, automatically corrected for intensity nonuniformity[105], and intensity normalized. Resulting images were skull-stripped, and non-isocortical structures were segmented using FSL FIRST[106]. Different tissue types (cortical and subcortical grey matter, white matter, cerebrospinal fluid) were segmented to perform anatomically constrained tractography[107]. Cortical surface segmentations were generated from

native T1w scans using FreeSurfer 6.0[95,108,109]. DWI data were pre-processed using MRtrix[110,111]. DWI data underwent b0 intensity normalization, and were corrected for susceptibility distortion, head motion, and eddy currents. Required anatomical features for tractography processing (*e.g.,* tissue type segmentations, parcellations) were non-linearly co-registered to native DWI space using the deformable SyN approach implemented in Advanced Neuroimaging Tools (ANTs)[112]. Diffusion processing and tractography were performed in native DWI space. We performed anatomically-constrained tractography using tissue types segmented from each participant's pre-processed T1w images registered to native DWI space[107]. We estimated multi-shell and multi-tissue response functions[113] and performed constrained spherical-deconvolution and intensity normalisation[114]. We initiated the tractogram with 40 million streamlines (maximum tract length=250; fractional anisotropy cutoff=0.06). We applied spherical deconvolution informed filtering of tractograms (SIFT2) to reconstruct whole brain streamlines weighted by cross-sectional multipliers[115]. The reconstructed cross-section streamlines were averaged within 400 spatially contiguous, functionally defined parcels[71], also warped to DWI space. The rs-fMRI images were pre-processed using AFNI[116] and FSL[106]. The first five volumes were discarded to ensure magnetic field saturation. Images were reoriented, motion corrected and distortion corrected. Nuisance variable signal was removed using an ICA-FIX classifier[117] and by performing spike regression. Native timeseries were mapped to individual surface models using a boundary-based registration[118] and smoothed using a Gaussian kernel (FWHM=10mm, smoothing performed on native midsurface mesh) using workbench[119]. For isocortical regions, timeseries were sampled on native surfaces and averaged within 400 spatially contiguous, functionally defined parcels[71]. For non-isocortical regions, timeseries were averaged within native parcellations of the nucleus accumbens, amygdala, caudate nucleus, hippocampus, pallidum, putamen, and thalamus[106].

MRI acquisition and processing – Secondary analyses

Secondary MRI analyses were conducted in 100 unrelated healthy adults (66 females, mean±SD age=28.8±3.8 years) from the minimally preprocessed S900 release of the Human Connectome Project (HCP) . MRI data were acquired on the HCP's custom 3T Siemens Skyra equipped with a 32-channel head coil. Two T1w images with identical parameters were acquired using a 3D-MPRAGE sequence (0.7mm isotropic voxels, TE=2.14ms, TI=1000ms, flip angle=8°, iPAT=2, matrix=320×320, 256 sagittal slices; TR=2400ms,). Two T2w images were acquired using a 3D T2-SPACE sequence with identical geometry (TR=3200ms, TE=565ms, variable flip angle, iPAT=2). A spin-echo EPI sequence was used to obtain diffusion weighted images, consisting of three shells with *b*-values 1000, 2000, and 3000s/mm^2 and up to 90 diffusion weighting directions per shell (TR=5520ms, TE=89.5ms, flip angle=78°, refocusing flip angle=160°, FOV=210×180, matrix=178×144, slice thickness=1.25mm, mb factor=3, echo spacing=0.78ms). Four rs-fMRI scans were acquired using multi-band accelerated 2D-BOLD echo-planar imaging (2mm isotropic voxels, TR=720ms, TE=33ms, flip angle=52°, matrix=104×90, 72 sagittal slices, multiband factor=8, 1200 volumes/scan, 3456 seconds). Only the first session was investigated in the present study. Participants were instructed to keep their eyes open, look at a fixation cross, and not fall

asleep. Nevertheless, some subjects were drowsy and may have fallen asleep[121], and the group-averages investigated in the present study do not address these inter-individual differences.

MRI data underwent HCP's minimal preprocessing[119]. Cortical surface models were constructed using Freesurfer 5.3-HCP[95,108,109], with minor modifications to incorporate both T1w and T2w[122]. Diffusion MRI data underwent correction for geometric distortions and head motion[119]. Tractographic analysis was based on MRtrix3[110,111]. Response functions for each tissue type were estimated using the dhollander algorithm[123]. Fibre orientation distributions (*i.e.*, the apparent density of fibres as a function of orientation) were modelled from the diffusion-weighted MRI with multi-shell multi-tissue spherical deconvolution[114], then values were normalised in the log domain to optimise the sum of all tissue compartments towards 1, under constraints of spatial smoothness. Anatomically constrained tractography was performed systematically by generating streamlines using second order integration over fibre orientation distributions with dynamic seeding[115,124]. Streamline generation was aborted when 40 million streamlines had been accepted. We applied spherical deconvolution informed filtering of tractograms (SIFT2) to reconstruct whole brain streamlines weighted by cross-sectional multipliers. The reconstructed cross-section streamlines were averaged within 400 spatially contiguous, functionally defined parcels[71], also warped to DWI space. The rs-fMRI timeseries were corrected for gradient nonlinearity, head motion, bias field and scanner drifts, then structured noise components were removed using ICA-FIX, further reducing the influence of motion, non-neuronal physiology, scanner artefacts and other nuisance sources[117]. The rs-fMRI data were resampled from volume to MSMAll functionally aligned surface space[125,126] and averaged within 400 spatially contiguous, functionally defined parcels[71].

Modelling structural connectivity with navigation efficiency

Extrinsic connectivity of DMN subunits was mapped using structural connectomes, derived from diffusion-based tractography. Edge weights of the structural connectomes, representing number of streamlines, were remapped using a log-based transformation: [$-\log10(W/(\max(W) + \min(W>0))$]. This log-based transformation attenuates extreme weights and ensures the maximum edge weight is mapped to a positive value. Euclidean distances were calculated between the centroid coordinate of each parcel. Communication in the structural connectome was modelled using navigation[69], also known as greedy routing[127]. Navigation combines the structural connectome with physical distances, providing a routing strategy that recapitulates invasive, tract-tracing measures of communication[68]. In brief, navigation involves step-wise progression from node i to node j, where each step is determined by spatial proximity to j. Navigation is the sum distances of the selected path and navigation efficiency (E_{nav}) its inverse; providing an intuitive metric of communication efficiency between two regions. Navigation efficiency was calculated within each hemisphere separately, then concatenated for analyses.

611 *Modelling functional input and output with effective connectivity*
612 The position of the DMN in large-scale cortical dynamics was explored with regression dynamic
613 causal modelling [rDCM;[70]], a scalable generative model of effective connectivity that allows
614 inferences on the directionality of signal flow, openly available as part of the TAPAS software
615 package[128]. The rDCM was implemented using individual rs-fMRI timeseries. Additionally, an
616 extended version of the rDCM was generated with non-isocortical regions, specifically the nucleus
617 accumbens, amygdala, caudate nucleus, hippocampus, pallidum, putamen, and thalamus.
618
619 *Influence of cytoarchitecture on connectivity*
620 Each parcel was labelled according to functional network, modal cortical type and, if part of the
621 DMN, average E1 value. Parcel-average E1 values were calculated by transforming the
622 parcellation scheme to the BigBrain surface and averaging within parcel[36,50]. The following
623 analyses were repeated for E_{nav}, effective connectivity derived input and effective connectivity
624 derived output.
625
626 First, we selected DMN rows and non-DMN columns of the connectivity matrix. Then, we
627 performed product-moment correlations between E1 and average connectivity to assess the
628 association of the cytoarchitectural axis with connectivity. Next, we stratified the non-DMN
629 columns by cortical type, averaged within type and calculated product-moment correlation
630 between type-average connectivity and E1, providing more specific insight into the relation of the
631 cytoarchitectural axis with connectivity of certain types of microcircuits. For each modality, the
632 correlations were compared to 10,000 spin permutations. P-values were Bonferroni corrected for
633 seven comparisons, resulting in significance threshold of $p<0.004$ (two-sided test with alpha value
634 of 0.05).
635
636 Finally, we estimated the imbalance in connectivity to each cortical type by calculating average
637 connectivity to each type, then calculating the Kullback–Leibler (KL) divergence from a null
638 model with equal average connectivity to each type. The imbalance analysis was repeated for each
639 functional network. In each case, only extrinsic connections were included in the calculations. For
640 each modality and each network, we tested whether the KL divergence value was lower than
641 10,000 spin permutations. P-values were Bonferroni corrected for seven comparisons, resulting in
642 significance threshold of $p<0.007$ (one-sided test with alpha value of 0.05).
643
644 *Individual-level replication with high-field MRI*
645 In the replication, we sought to address two key limitations of the primary analyses. First, due to
646 the unique nature of the BigBrain dataset, cytoarchitectural mapping was based on a single
647 individual, limiting our knowledge of the generalisability of the discovered patterns. Secondly,
648 structural and functional connectivity measurements represented population-averages, thus we
649 were not able to conclude whether the discovered correspondences between cytoarchitecture and

connectivity are evident within an individual. To overcome these limitations, we sought to replicate key findings at an individual-level using high-resolution, ultrahigh-field MRI.

Individual-level replication analyses were conducted on 8 healthy adults (5 females, mean±SD age=28±6.3, 1 left-handed). Scans were completed at the Brain Imaging Centre of the Montreal Neurological Institute and Hospital on a 7T Siemens Magnetom Terra System equipped with a 32/8 channel receive/transmit head coil. Two qT1 scans were acquired across two scanning sessions with identical 3D-MP2RAGE sequences (0.5mm isotropic voxels, TR=5170ms, TE=2.44ms, $T1_{1/2}$=1000/3200ms, flip angles=4°, matrix=488×488, slice thickness=0.5mm, partial Fourier=0.75). qT1 maps from the second session were linearly registered to the qT1 maps from the first session, then averaged, to enhanced the signal to noise ratio. A spin-echo echo-planar imaging sequence with multi-band acceleration was used to obtain DWI data, consisting of three shells with b-values 300, 700, and 2000s/mm^2 and 10, 40, and 90 diffusion weighting directions per shell, respectively (1.1mm isotropic voxels, TR=7383ms, TE=70.6ms, flip angle=90°, matrix=192×192, slice thickness=1.1mm, multiband factor=2, echo spacing=0.26ms, number of b0 images=3, partial Fourier=0.75). One 6 min rs-fMRI scan was acquired using multi-echo, multiband accelerated 2D-BOLD echo-planar imaging (1.9mm isotropic voxels, TR=1690ms, $TE_{1/2/3}$=10.8/27.3/43.8ms, flip angle=67°, matrix=118x118, multiband factor=3, echo spacing=0.54ms, partial Fourier=0.75). Participants were instructed to keep their eyes open, look at a fixation cross, and not fall asleep. Two multiband accelerated spin-echo images with reverse phase encoding were also acquired for distortion correction of the rs-fMRI scans.

The 7T dataset was processed in the same manner as the primary MRI dataset, with two exceptions. qT1 maps were used, rather than T1w images, to construct cortical surfaces, and nuisance variable signal was removed from rs-fMRI using an approach that is specially tailored to multi-echo fMRI ("tedana")[129], instead of ICA-FIX, which is optimsed for single-echo data. Subsequently, we extracted intracortical profiles from qT1 volumes and determined the principal eigenvector of microstructural differentiation (E1) for each individual using the same procedure as for the histological data.

The replication focused on three key results from the primary analysis: (i) DMN subregions differ in terms of the topography of microarchitectural differentiation, which is evident in the roughness of E1. In particular, subregions vary from a gradient in the mesiotemporal lobe to a fluctuating landscape in the prefrontal cortex. (ii) Navigation efficiency decreases along E1, and this effect is especially pronounced for perceptually-coupled cortical types (koniocortical and eulaminate III). (iii) Functional input decreases along E1. For each result, we compared statistical outcomes of the primary analysis, derived from BigBrain and population-average connectivity, with individual-level statistical outcomes, derived from the 7T dataset, using product-moment correlations. We report rho and p-values averaged across individuals.

DATA AVAILABILITY

All data that support the findings of this study are openly available. BigBrain is available with LORIS (https://bigbrain.loris.ca/main.php) with preprocessed BigBrain data available in through the BigBrainWarp GitHub repository (https://github.com/caseypaquola/BigBrainWarp). The MICS dataset is available with CONP Portal (https://portal.conp.ca/dataset?id=projects/mica-mics) and the HCP dataset is available with Connectome DB (https://db.humanconnectome.org/).

CODE AVAILABILITY

Custom code for this study, as well as data necessary for reproduction, are openly available on GitHub (https://github.com/caseypaquola/DMN).

REFERENCES

1. Power, J. D. *et al.* Functional network organization of the human brain. *Neuron* **72**, 665–78 (2011).
2. Yeo, B. T. T. *et al.* The organization of the human cerebral cortex estimated by intrinsic functional connectivity. *J. Neurophysiol.* **106**, 1125–1165 (2011).
3. Greicius, M. D., Krasnow, B., Reiss, A. L. & Menon, V. Functional connectivity in the resting brain: A network analysis of the default mode hypothesis. *Proc. Natl. Acad. Sci.* **100**, 253–258 (2003).
4. Shulman, G. L. *et al.* Common Blood Flow Changes across Visual Tasks: II. Decreases in Cerebral Cortex. *J. Cogn. Neurosci.* **9**, 648–663 (1997).
5. Raichle, M. E. *et al.* A default mode of brain function. *Proc. Natl. Acad. Sci. U. S. A.* **98**, 676–682 (2001).
6. Gusnard, D. A., Akbudak, E., Shulman, G. L. & Raichle, M. E. Medial prefrontal cortex and self-referential mental activity: Relation to a default mode of brain function. *Proc. Natl. Acad. Sci. U. S. A.* **98**, 4259–4264 (2001).
7. Irish, M. & Vatansever, D. Rethinking the episodic-semantic distinction from a gradient perspective. *Curr. Opin. Behav. Sci.* **32**, 43–49 (2020).
8. Kucyi, A. & Davis, K. D. Dynamic functional connectivity of the default mode network tracks daydreaming. *NeuroImage* **100**, 471–480 (2014).
9. Vatansever, D., Menon, D. K. & Stamatakis, E. A. Default mode contributions to automated information processing. *Proc. Natl. Acad. Sci. U. S. A.* **114**, 12821–12826 (2017).
10. Wise, R. J. S. & Braga, R. M. Default mode network: the seat of literary creativity? *Trends Cogn. Sci.* **18**, 116–117 (2014).
11. Lanzoni, L. *et al.* The role of default mode network in semantic cue integration. *NeuroImage* **219**, 117019–117019 (2020).
12. Schilbach, L., Eickhoff, S. B., Rotarska-Jagiela, A., Fink, G. R. & Vogeley, K. Minds at rest? Social cognition as the default mode of cognizing and its putative relationship to the 'default system' of the brain. *Conscious. Cogn.* **17**, 457–467 (2008).
13. Koban, L., Gianaros, P. J., Kober, H. & Wager, T. D. The self in context: brain systems linking mental and physical health. *Nat. Rev. Neurosci. 2021 225* **22**, 309–322 (2021).
14. Spetsieris, P. G. *et al.* Metabolic resting-state brain networks in health and disease. *Proc. Natl. Acad. Sci. U. S. A.* **112**, 2563–2568 (2015).
15. Raichle, M. E. The brain's default mode network. *Annu Rev Neurosci* **38**, 433–447 (2015).
16. Buckner, R. L. & DiNicola, L. M. The brain's default network: updated anatomy, physiology and evolving insights. *Nat. Rev. Neurosci.* **20**, 593–608 (2019).
17. Simony, E. *et al.* Dynamic reconfiguration of the default mode network during narrative comprehension. *Nat. Commun.* **7**, 12141–12141 (2016).

18. Yeshurun, Y., Nguyen, M. & Hasson, U. Amplification of local changes along the timescale processing hierarchy. *Proc. Natl. Acad. Sci. U. S. A.* **114**, 9475–9480 (2017).
19. Murphy, C. *et al.* Modes of operation: A topographic neural gradient supporting stimulus dependent and independent cognition. *NeuroImage* **186**, 487–496 (2019).
20. Braga, R. M., Sharp, D. J., Leeson, C., Wise, R. J. S. & Leech, R. Echoes of the brain within default mode, association, and heteromodal cortices. *J. Neurosci. Off. J. Soc. Neurosci.* **33**, 14031–9 (2013).
21. Spreng, R. N., Stevens, W. D., Chamberlain, J. P., Gilmore, A. W. & Schacter, D. L. Default network activity, coupled with the frontoparietal control network, supports goal-directed cognition. *NeuroImage* **53**, 303–317 (2010).
22. Finc, K. *et al.* Dynamic reconfiguration of functional brain networks during working memory training. *Nat. Commun.* **11**, 2435 (2020).
23. Murphy, C. *et al.* Distant from input: Evidence of regions within the default mode network supporting perceptually-decoupled and conceptually-guided cognition. *NeuroImage* **171**, 393–401 (2018).
24. Christoff, K., Gordon, A. M., Smallwood, J., Smith, R. & Schooler, J. W. Experience sampling during fMRI reveals default network and executive system contributions to mind wandering. *Proc. Natl. Acad. Sci. U. S. A.* **106**, 8719–8724 (2009).
25. Karapanagiotidis, T., Bernhardt, B. C., Jefferies, E. & Smallwood, J. Tracking thoughts: Exploring the neural architecture of mental time travel during mind-wandering. *NeuroImage* **147**, 272–281 (2017).
26. Mason, M. F. *et al.* Wandering minds: The default network and stimulus-independent thought. *Science* **315**, 393–395 (2007).
27. Smallwood, J. *et al.* The default mode network in cognition: a topographical perspective. *Nat. Rev. Neurosci. 2021 228* **22**, 503–513 (2021).
28. Paquola, C., Amunts, K., Evans, A., Smallwood, J. & Bernhardt, B. Closing the mechanistic gap: the value of microarchitecture in understanding cognitive networks. *Trends Cogn. Sci.* (2022) doi:10.1016/j.tics.2022.07.001.
29. Margulies, D. S. *et al.* Situating the default-mode network along a principal gradient of macroscale cortical organization. *Proc. Natl. Acad. Sci.* **113**, 12574–12579 (2016).
30. Brincat, S. L., Siegel, M., Von Nicolai, C. & Miller, E. K. Gradual progression from sensory to task-related processing in cerebral cortex. (2018) doi:10.1073/pnas.1717075115.
31. Hirabayashi, T. & Miyashita, Y. Computational principles of microcircuits for visual object processing in the macaque temporal cortex. *Trends Neurosci.* **37**, 178–187 (2014).
32. Bechtel, W. & Abrahamsen, A. Explanation: A mechanist alternative. *Stud. Hist. Philos. Sci. Part C Stud. Hist. Philos. Biol. Biomed. Sci.* **36**, 421–441 (2005).
33. García-Cabezas, M. Á., Hacker, J. L. & Zikopoulos, B. A Protocol for Cortical Type Analysis of the Human Neocortex Applied on Histological Samples, the Atlas of Von Economo and Koskinas, and Magnetic Resonance Imaging. *Front. Neuroanat.* **14**, 576015 (2020).
34. Von Economo, C. & Koskinas, G. *Die Cytoarchitektonik der Hirnrinde des erwachsenen Menschen*. (Springer, 1925).
35. Amunts, K. *et al.* BigBrain: An Ultrahigh-Resolution 3D Human Brain Model. *Science* **340**, 1472–1475 (2013).
36. Paquola, C. *et al.* The BigBrainWarp toolbox for integration of BigBrain 3D histology with multimodal neuroimaging. *eLife* **10**, e70119 (2021).
37. Spreng, R. N. & Grady, C. L. Patterns of Brain Activity Supporting Autobiographical Memory, Prospection, and Theory of Mind, and Their Relationship to the Default Mode Network. *J. Cogn. Neurosci.* **22**, 1112–1123 (2010).
38. Andrews-Hanna, J. R., Reidler, J. S., Sepulcre, J., Poulin, R. & Buckner, R. L. Functional-Anatomic Fractionation of the Brain's Default Network. *Neuron* **65**, 550–562 (2010).
39. Barbas, H. & Rempel-Clower, N. Cortical structure predicts the pattern of corticocortical connections. *Cereb. Cortex* **7**, 635–646 (1997).

40. Barbas, H. Pattern in the laminar origin of corticocortical connections. *J. Comp. Neurol.* **252**, 415–422 (1986).
41. Hilgetag, C. C., Medalla, M., Beul, S. F. & Barbas, H. The primate connectome in context: Principles of connections of the cortical visual system. *NeuroImage* **134**, 685–702 (2016).
42. Hilgetag, C. C. & Goulas, A. 'Hierarchy' in the organization of brain networks. *Philos. Trans. R. Soc. B Biol. Sci.* **375**, 20190319 (2020).
43. Markov, N. T. *et al.* Anatomy of hierarchy: Feedforward and feedback pathways in macaque visual cortex. *J. Comp. Neurol.* **522**, 225–259 (2014).
44. Vezoli, J. *et al.* Cortical hierarchy, dual counterstream architecture and the importance of top-down generative networks. *NeuroImage* **225**, 117479 (2021).
45. Felleman, D. J. & Van Essen, D. C. Distributed hierarchical processing in the primate cerebral cortex. *Cereb. Cortex* **1**, 1–47 (1991).
46. Godlove, D. C., Maier, A., Woodman, G. F. & Schall, J. D. Microcircuitry of Agranular Frontal Cortex: Testing the Generality of the Canonical Cortical Microcircuit. *J. Neurosci.* **34**, 5355–5369 (2014).
47. Mesulam, M.-M. From sensation to cognition. *Brain* **121**, 1013–1052 (1998).
48. Pandya, D., Seltzer, B., Petrides, M. & Cipolloni, P. B. *Cerebral Cortex: Architecture, Connections and the Dual Origin Concept*. (Oxford University Press, 2015). doi:10.1093/med/9780195385151.001.0001.
49. Gadelmawla, E. S., Koura, M. M., Maksoud, T. M. A., Elewa, I. M. & Soliman, H. H. Roughness parameters. *J. Mater. Process. Technol.* **123**, 133–145 (2002).
50. Lewis, L. B. *et al.* A multimodal surface matching (MSM) surface registration pipeline to bridge atlases across the MNI and the Freesurfer/Human Connectome Project Worlds. in (2020).
51. Coifman, R. R. & Lafon, S. Diffusion maps. *Appl. Comput. Harmon. Anal.* **21**, 5–30 (2006).
52. Paquola, C. *et al.* Microstructural and functional gradients are increasingly dissociated in transmodal cortices. *PLoS Biol.* **17**, e3000284–e3000284 (2019).
53. Cahalane, D. J., Charvet, C. J. & Finlay, B. L. Systematic, balancing gradients in neuron density and number across the primate isocortex. *Front. Neuroanat.* **6**, 28 (2012).
54. Goldman-Rakic, P. S. Topography of Cognition: Parallel Distributed Networks in Primate Association Cortex. *Annu. Rev. Neurosci.* **11**, 137–156 (1988).
55. Buckner, R. L. & Krienen, F. M. The evolution of distributed association networks in the human brain. *Trends Cogn. Sci.* **17**, 648–665 (2013).
56. Schüz, A. & Braitenberg, V. The Human Cortical White Matter: Quantitative Aspects of Cortico-Cortical Long-Range Connectivity. in *Cortical Areas* (CRC Press, 2002).
57. Anon. Surface Texture: Surface Roughness, Waviness and Lay. *ANSI Stand B46 1* (1978).
58. Paquola, C. *et al.* Convergence of cortical types and functional motifs in the human mesiotemporal lobe. *eLife* **9**, e60673 (2020).
59. Braak, H. & Braak, E. On areas of transition between entorhinal allocortex and temporal isocortex in the human brain. Normal morphology and lamina-specific pathology in Alzheimer's disease. *Acta Neuropathol. (Berl.)* **68**, 325–332 (1985).
60. Goldman-Rakic, P. S. & Schwartz, M. L. Interdigitation of contralateral and ipsilateral columnar projections to frontal association cortex in primates. *Science* **216**, 755–7 (1982).
61. Selemon, L. D. & Goldman-Rakic, P. S. Common Cortical and Subcortical Targets of the Dorsolateral Prefrontal and Posterior Parietal Cortices in the Rhesus Monkey: Evidence for a Distributed Neural Network Subserving Spatially Guided Behavior. *J. Neurosci.* **8**, 4049–4088 (1988).
62. Braga, R. M. & Buckner, R. L. Parallel Interdigitated Distributed Networks within the Individual Estimated by Intrinsic Functional Connectivity. *Neuron* **95**, 457-471.e5 (2017).
63. Jones, E. G. & Powell, T. P. S. An anatomical study of converging sensory pathways within the cerebral cortex of the monkey. *Brain* **93**, 793–820 (1970).

64. Binney, R. J., Parker, G. J. M. & Lambon Ralph, M. A. Convergent connectivity and graded specialization in the rostral human temporal lobe as revealed by diffusion-weighted imaging probabilistic tractography. *J. Cogn. Neurosci.* **24**, 1998–2014 (2012).
65. Hilgetag, C. C. & Grant, S. Cytoarchitectural differences are a key determinant of laminar projection origins in the visual cortex. *NeuroImage* **51**, 1006–1017 (2010).
66. Goulas, A., Margulies, D. S., Bezgin, G. & Hilgetag, C. C. The architecture of mammalian cortical connectomes in light of the theory of the dual origin of the cerebral cortex. *Cortex* **118**, 244–261 (2019).
67. Barbas, H. General Cortical and Special Prefrontal Connections: Principles from Structure to Function. *Annu. Rev. Neurosci.* **38**, 269–289 (2015).
68. Seguin, C., Razi, A. & Zalesky, A. Inferring neural signalling directionality from undirected structural connectomes. *Nat. Commun.* **10**, 1–13 (2019).
69. Seguin, C., Van Den Heuvel, M. P. & Zalesky, A. Navigation of brain networks. *Proc. Natl. Acad. Sci. U. S. A.* **115**, 6297–6302 (2018).
70. Frässle, S. *et al.* Regression DCM for fMRI. *NeuroImage* **155**, 406–421 (2017).
71. Schaefer, A. *et al.* Local-Global Parcellation of the Human Cerebral Cortex from Intrinsic Functional Connectivity MRI. *Cereb. Cortex N. Y. N 1991* **28**, 3095–3114 (2018).
72. Hellwig, B. How the myelin picture of the human cerebral cortex can be computed from cytoarchitectural data. A bridge between von Economo and Vogt. *J. Hirnforsch.* **34**, 387–402 (1993).
73. Sanides, F. The Cyto-myeloarchitecture of the Human Frontal Lobe and its Relation to Phylogenetic Differentiation of the Cerebral Cortex. *J. Für Hirnforsch.* **6**, 269–282 (1964).
74. Paquola, C. & Hong, S.-J. The potential of myelin-sensitive imaging: Redefining spatiotemporal patterns of myeloarchitecture. *Biol. Psychiatry* (2022) doi:10.1016/j.biopsych.2022.08.031.
75. Chalfie, M. *et al.* The neural circuit for touch sensitivity in Caenorhabditis elegans. *J. Neurosci. Off. J. Soc. Neurosci.* **5**, 956–964 (1985).
76. García-Cabezas, M. Á., Zikopoulos, B. & Barbas, H. The Structural Model: a theory linking connections, plasticity, pathology, development and evolution of the cerebral cortex. *Brain Struct. Funct.* **224**, 985–1008 (2019).
77. Smith, V., Mitchell, D. J. & Duncan, J. Role of the Default Mode Network in Cognitive Transitions. *Cereb. Cortex* **28**, 3685–3696 (2018).
78. Zhang, M. *et al.* Perceptual coupling and decoupling of the default mode network during mind-wandering and reading. *eLife* **11**, e74011 (2022).
79. Sepulcre, J., Sabuncu, M. R., Yeo, T. B., Liu, H. & Johnson, K. A. Stepwise connectivity of the modal cortex reveals the multimodal organization of the human brain. *J. Neurosci.* **32**, 10649–10661 (2012).
80. Duncan, J. The multiple-demand (MD) system of the primate brain: mental programs for intelligent behaviour. *Trends Cogn. Sci.* **14**, 172–179 (2010).
81. Braga, R. M., DiNicola, L. M., Becker, H. C. & Buckner, R. L. Situating the left-lateralized language network in the broader organization of multiple specialized large-scale distributed networks. *J. Neurophysiol.* **124**, 1415–1448 (2020).
82. DiNicola, L. M. & Buckner, R. L. Precision estimates of parallel distributed association networks: evidence for domain specialization and implications for evolution and development. *Curr. Opin. Behav. Sci.* **40**, 120–129 (2021).
83. Chaudhuri, R., Knoblauch, K., Gariel, M.-A., Kennedy, H. & Wang, X.-J. A Large-Scale Circuit Mechanism for Hierarchical Dynamical Processing in the Primate Cortex. *Neuron* **88**, 419–431 (2015).
84. Murray, J. D. *et al.* A hierarchy of intrinsic timescales across primate cortex. *Nat. Neurosci.* **17**, 1661–3 (2014).
85. Yeshurun, Y., Nguyen, M. & Hasson, U. The default mode network: where the idiosyncratic self meets the shared social world. *Nat. Rev. Neurosci.* **22**, 181–192 (2021).

86. Merker, B. Silver staining of cell bodies by means of physical development. *J. Neurosci. Methods* **9**, 235–241 (1983).
87. Lepage, C. Y. *et al.* Automatic Repair of Acquisition Defects in Reconstruction of Histology Sections of a Human Brain. in *Annual Meeting of the Organization for Human Brain Mapping* (2010).
88. Mohlberg, H., Tweddell, B., Lippert, T. & Amunts, K. Workflows for Ultra-High Resolution 3D Models of the Human Brain on Massively Parallel Supercomputers. in 15–27 (Springer, Cham, 2016). doi:10.1007/978-3-319-50862-7_2.
89. Lewis, L. B. *et al.* BigBrain: Initial Tissue Classification and Surface Extraction. in (2014).
90. Wagstyl, K., Paquola, C., Bethlehem, R. & Huth, A. kwagstyl/surface_tools: Initial release of equivolumetric surfaces. (2018) doi:10.5281/ZENODO.1412054.
91. Waehnert, M. D. *et al.* Anatomically motivated modeling of cortical laminae. *NeuroImage* **93**, 210–220 (2014).
92. Taubin, G. Curve and surface smoothing without shrinkage. in *IEEE International Conference on Computer Vision* 852–857 (IEEE, 1995). doi:10.1109/iccv.1995.466848.
93. Worsley, K. *et al.* SurfStat: A Matlab toolbox for the statistical analysis of univariate andmultivariate surface and volumetric data using linear mixed effects modelsand random field theory. in *Human Brain Mapping* (2009).
94. Scholtens, L. H., de Reus, M. A., de Lange, S. C., Schmidt, R. & van den Heuvel, M. P. An MRI Von Economo - Koskinas atlas. *NeuroImage* (2016) doi:10.1016/j.neuroimage.2016.12.069.
95. Dale, A. M., Fischl, B. & Sereno, M. I. Cortical surface-based analysis. I. Segmentation and surface reconstruction. *Neuroimage* **9**, 179–194 (1999).
96. Vos de Wael, R. *et al.* BrainSpace: a toolbox for the analysis of macroscale gradients in neuroimaging and connectomics datasets. *Commun. Biol.* **3**, 103 (2020).
97. Alexander-Bloch, A. F. *et al.* On testing for spatial correspondence between maps of human brain structure and function. *NeuroImage* **178**, 540–551 (2018).
98. Eklund, A., Nichols, T. E. & Knutsson, H. Cluster failure: Why fMRI inferences for spatial extent have inflated false-positive rates. *Proc Natl Acad Sci U A* **113**, 7900–7905 (2016).
99. Kong, R. *et al.* Spatial Topography of Individual-Specific Cortical Networks Predicts Human Cognition, Personality, and Emotion. *Cereb. Cortex* **29**, 2533–2551 (2019).
100. Tenenbaum, J. B., De Silva, V. & Langford, J. C. A global geometric framework for nonlinear dimensionality reduction. *Science* **290**, 2319–23 (2000).
101. Von Luxburg, U. A tutorial on spectral clustering. *Stat. Comput.* **17**, 395–416 (2007).
102. D'Errico, J. polyfitn. (2023).
103. Royer, J. *et al.* An Open MRI Dataset for Multiscale Neuroscience. *bioRxiv* (2021) doi:10.1101/2021.08.04.454795.
104. Cruces, R. R. *et al.* Micapipe: A pipeline for multimodal neuroimaging and connectome analysis. *NeuroImage* **263**, 119612 (2022).
105. Tustison, N. J. & Avants, B. B. Explicit B-spline regularization in diffeomorphic image registration. *Front. Neuroinformatics* **7**, 39–39 (2013).
106. Jenkinson, M., Beckmann, C. F., Behrens, T. E., Woolrich, M. W. & Smith, S. M. Fsl. *Neuroimage* **62**, 782–790 (2012).
107. Smith, R. E., Tournier, J.-D., Calamante, F. & Connelly, A. Anatomically-constrained tractography: improved diffusion MRI streamlines tractography through effective use of anatomical information. *NeuroImage* **62**, 1924–38 (2012).
108. Fischl, B., Sereno, M. I. & Dale, A. M. Cortical surface-based analysis. II: Inflation, flattening, and a surface-based coordinate system. *Neuroimage* **9**, 195–207 (1999).
109. Fischl, B., Sereno, M. I., Tootell, R. B. & Dale, A. M. High-resolution intersubject averaging and a coordinate system for the cortical surface. *Hum. Brain Mapp.* **8**, 272–284 (1999).
110. Tournier, J.-D., Calamante, F. & Connelly, A. MRtrix: diffusion tractography in crossing fiber regions. *Int. J. Imaging Syst. Technol.* **22**, 53–66 (2012).

111. Tournier, J.-D. *et al.* MRtrix3: A fast, flexible and open software framework for medical image processing and visualisation. *NeuroImage* 116137–116137 (2019).
112. Avants, B. B., Epstein, C. L., Grossman, M. & Gee, J. C. Symmetric diffeomorphic image registration with cross-correlation: Evaluating automated labeling of elderly and neurodegenerative brain. *Med. Image Anal.* **12**, 26–41 (2008).
113. Christiaens, D. *et al.* Global tractography of multi-shell diffusion-weighted imaging data using a multi-tissue model. *Neuroimage* **123**, 89–101 (2015).
114. Jeurissen, B., Tournier, J.-D., Dhollander, T., Connelly, A. & Sijbers, J. Multi-tissue constrained spherical deconvolution for improved analysis of multi-shell diffusion MRI data. *NeuroImage* **103**, 411–426 (2014).
115. Smith, R. E., Tournier, J. D., Calamante, F. & Connelly, A. SIFT2: Enabling dense quantitative assessment of brain white matter connectivity using streamlines tractography. *NeuroImage* **119**, 338–351 (2015).
116. Cox, R. W. AFNI: software for analysis and visualization of functional magnetic resonance neuroimages. *Comput. Biomed. Res.* **29**, 162–173 (1996).
117. Salimi-Khorshidi, G. *et al.* Automatic denoising of functional MRI data: Combining independent component analysis and hierarchical fusion of classifiers. *NeuroImage* **90**, 449–468 (2014).
118. Greve, D. N. & Fischl, B. Accurate and robust brain image alignment using boundary-based registration. *NeuroImage* **48**, 63–72 (2009).
119. Glasser, M. F. *et al.* The minimal preprocessing pipelines for the Human Connectome Project. *NeuroImage* **80**, 105–124 (2013).
120. Van Essen, D. C. *et al.* The WU-Minn Human Connectome Project: An overview. *NeuroImage* **80**, 62–79 (2013).
121. Glasser, M. F. *et al.* Using temporal ICA to selectively remove global noise while preserving global signal in functional MRI data. *NeuroImage* **181**, 692–717 (2018).
122. Glasser, M. F. & Van Essen, D. C. Mapping human cortical areas in vivo based on myelin content as revealed by T1- and T2-weighted MRI. *J. Neurosci. Off. J. Soc. Neurosci.* **31**, 11597–616 (2011).
123. Dhollander, T., Raffelt, D. & Connelly, A. Unsupervised 3-tissue response function estimation from single-shell or multi-shell diffusion MR data without a co-registered T1 image. in *ISMRM Workshop on Breaking the Barriers of Diffusion MRI* 5–5 (2016).
124. Tournier, J. D., Calamante, F. & Connelly, A. Robust determination of the fibre orientation distribution in diffusion MRI: Non-negativity constrained super-resolved spherical deconvolution. *NeuroImage* **35**, 1459–1472 (2007).
125. Robinson, E. C. *et al.* MSM: A new flexible framework for multimodal surface matching. *NeuroImage* **100**, 414–426 (2014).
126. Robinson, E. C. *et al.* Multimodal surface matching with higher-order smoothness constraints. *NeuroImage* **167**, 453–465 (2018).
127. Muscoloni, A., Thomas, J. M., Ciucci, S., Bianconi, G. & Cannistraci, C. V. Machine learning meets complex networks via coalescent embedding in the hyperbolic space. *Nat. Commun.* **8**, 1–19 (2017).
128. Frässle, S. *et al.* TAPAS: An Open-Source Software Package for Translational Neuromodeling and Computational Psychiatry. *Front. Psychiatry* **12**, (2021).
129. DuPre, E. *et al.* TE-dependent analysis of multi-echo fMRI with *tedana*. *J. Open Source Softw.* **6**, 3669 (2021).
130. Salo, T. *et al.* NiMARE: Neuroimaging Meta-Analysis Research Environment. *NeuroLibre Reprod. Prepr. Serv.* **1**, 7 (2022).
131. Yarkoni, T., Poldrack, R. A., Nichols, T. E., Van Essen, D. C. & Wager, T. D. Large-scale automated synthesis of human functional neuroimaging data. *Nat. Methods* **8**, 665–670 (2011).
132. Smith, S. M. *et al.* Correspondence of the brain's functional architecture during activation and rest. *Proc. Natl. Acad. Sci. U. S. A.* **106**, 13040–5 (2009).

SUPPLEMENTARY INFORMATION

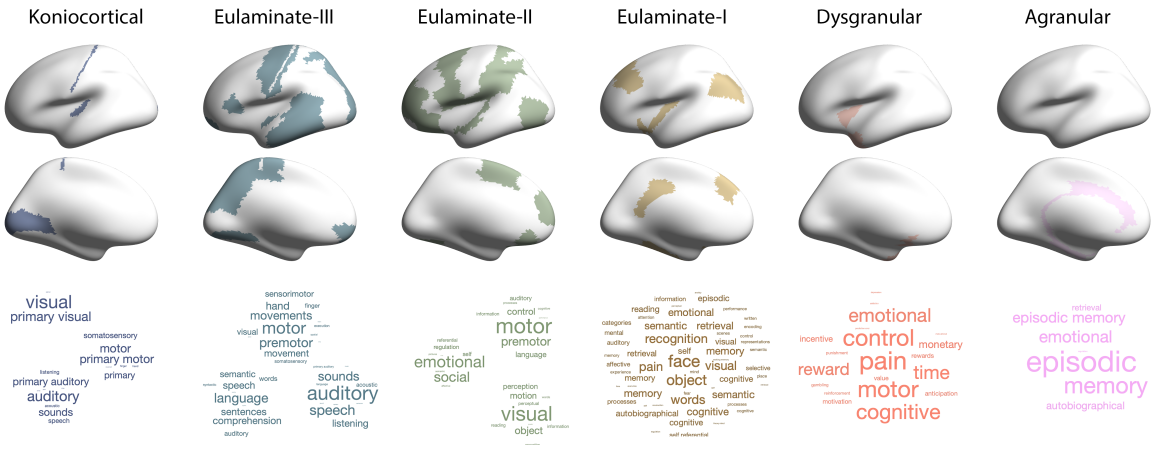

Supplementary Figure 1: Meta-analytic functional decoding of the cortical type atlas supports the association, described in literature reviews[47], between the gradient of cortical types and a shift in function from primary sensory to unimodal to heteromodal to memory-related processes. Using meta-analytic maps of thousands of functional MRI[130,131], we extracted terms that were consistently associated with increased activity within the specific cortical type (threshold z-statistic>2). The size of each word reflects the relative strength of its association with the cortical type. Only psychological constructs were retained in the term lists (thus excluding anatomical terms, e.g. "V1", and experiment-related terms, e.g. "healthy controls"). Decoding was performed within spatially contiguous subregions for Kon, Eu-III and Eu-II, because no terms exceeded the threshold when the subregions were combined, due to the distinctive unimodal functions of each subregion.

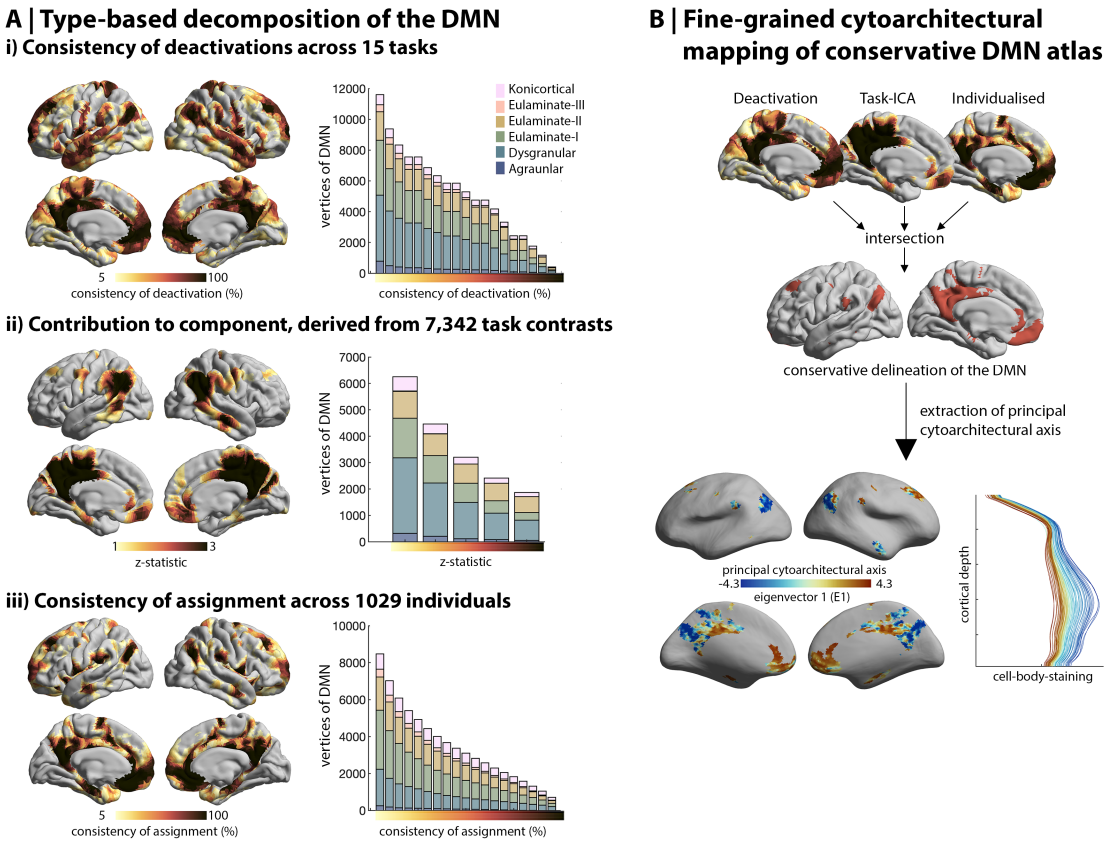

Supplementary Figure 2: Cytoarchitectural heterogeneity in the DMN replicated with alternative atlases. A) The diverse cytoarchitectural composition of the DMN was also evident using alternative atlas definitions. Stacked boxplots illustrate the number of vertices assigned to each cortical type within the atlas with increasingly conservative thresholds for inclusion in the DMN represented along the x-axis. **i)** DMN based on consistency of deactivation during perceptually-driven tasks. Vertex-wise change in the BOLD response were calculated across 787 subjects in Human Connectome Project during fifteen perceptually-driven tasks. Surface projections show the consistency of deactivations ($z \leq -5$) across the tasks[27]. **ii)** Association (z-statistic) of each vertex to the DMN derived from an independent component analysis of 7,342 task contrasts[132]. **iii)** Probability of the DMN at each vertex, calculated across 1029 individual-specific functional network delineations[99]. Proportion of the DMN assigned to each cortical type, where the DMN is defined variably based on different consistency thresholds. **B)** Using an intersection of the three approaches in part A, we created a highly conservative delineation of the DMN. Specifically, vertices were included in the conservative atlas if (i) deactivations were observed in more than a quarter of perceptually-driven tasks, (ii) contribution to the task-ICA exceeded a z-statistic of 1 and (iii) assignment to the DMN was observed in more than a quarter of individuals. Subsequently, we replicated the procedure in the primary analysis to extract the principal cytoarchitectural axis. Notably, similar patterns of cytoarchitectural differentiation are evident in this conservative delineation of the DMN. The conservative cytoarchitectural axis also captures a variation from peaked to flat profiles.

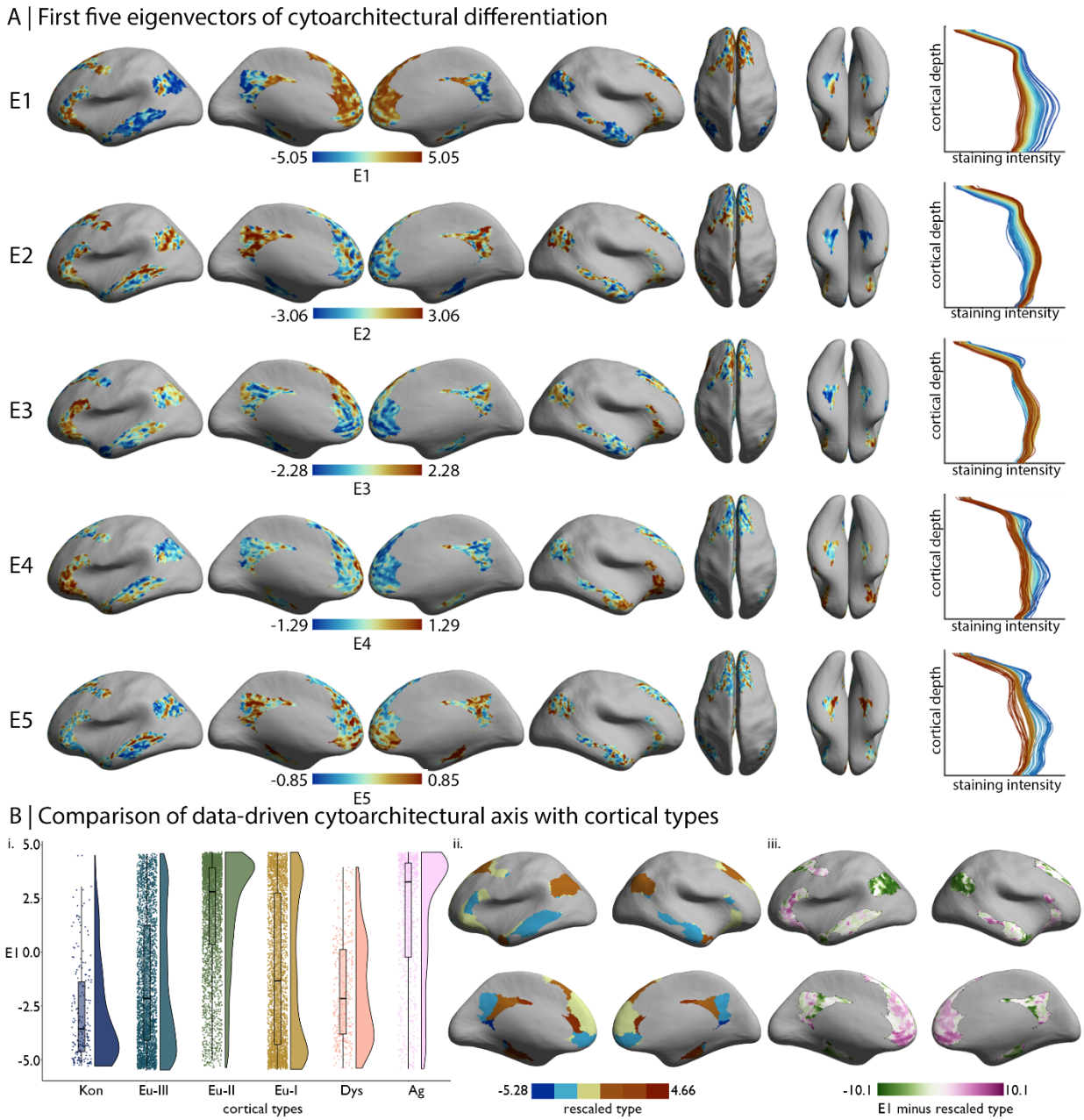

Supplementary Figure 3: A) First five eigenvectors projected on the inflated BigBrain surface. For line plots on the right, staining intensity profiles were averaged within 100 bins of the respective eigenvector and coloured by eigenvector position. **B) i.** Raincloud plot shows the distribution of E1 across cortical types. **ii.** Cortical type assignment (1:6) was rescaled to the range of E1 then subtracted from E1, producing a deviation map that highlights where the type-based and data-driven depictions of DMN cytoarchitecture differ. Negative values indicate lower E1 than expected by a linear relationship with cortical type, whereas positive values indicate higher than predicted E1. Thus, the E1 pattern is distinct to the gradient of laminar elaboration that is captured by the cortical types. Both are anchored by koniocortex on one side and agranular cortex on the other, but they differ in the ordering of eulaminate and dysgranular areas.

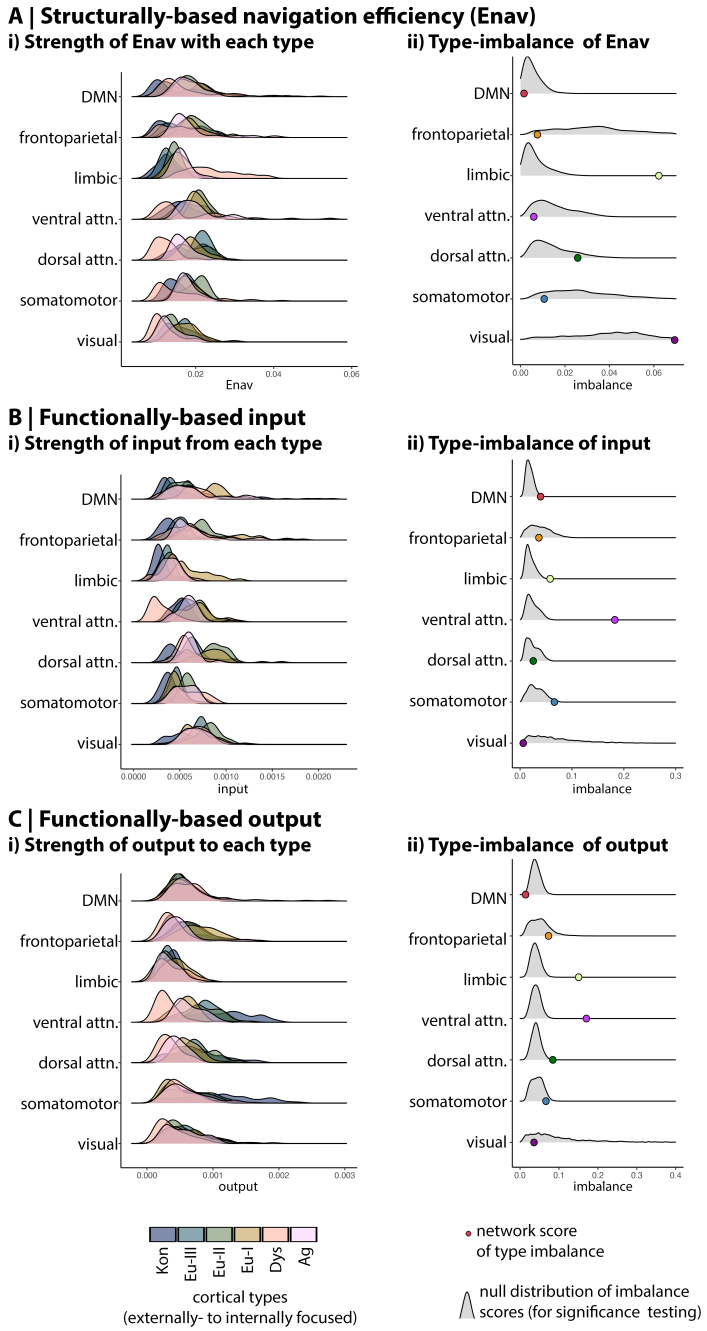

Supplementary Figure 4: Comparison of functional networks based on extrinsic connectivity to different cortical types. Coloured ridge plots on the left of each panel show probability distributions of connectivity between the functional networks and extrinsic cortical types. We evaluated the imbalance of connectivity across cortical types using the Kullback-Leibler (KL) divergence from a null model with equal connectivity to each type. On the right of each panel, coloured dots show the empirical KL divergence for each network and the grey density plots show the null distribution of KL divergence values based on 10,000 spin permutations. **A)** The DMN exhibits the most balanced navigation efficiency across cortical types, compared to other functional networks. The balance of the DMN did not reach a level of significance relative to spin permutations, but spin permutations account for the size and distribution of the network, thus we may infer it is the large size and wide distribution of the network that enable the DMN to strike a balance in communication across cortical types. **B)** Input to the DMN is not balanced with regards to cortical types. Stronger input comes from heteromodal, eulaminate I cortex, which aligns with the over-representation

of this cortical type within the DMN. **C)** The DMN is unique amongst functional networks in exhibiting balanced output to all cortical types, which is further supported by the balance of the DMN reaching significance in spin permutation testing.

1050 **Supplementary Table 1: Cortical types by functional network**
1051

	Kon	Eu-III	Eu-II	Eu-I	Dys	Ag	Total vertices	KS statistic[1]
Visual	0.29	0.41	0.17	0.10	0	0.03	2750	0.36, p<0.001
Somatomotor	0.10	0.54	0.31	0.04	<0.01	0.01	3751	0.20, p<0.001
DAN	<0.01	0.40	0.53	0.06	0	0	2188	0.29, p<0.001
VAN	0.02	0.18	0.50	0.13	0.08	0.09	2285	0.13, p<0.001
Limbic	0	0.24	0.28	0.11	0.26	0.10	1426	0.27, p<0.001
Frontoparietal	0	0.18	0.56	0.23	<0.01	0.04	2314	0.11, p<0.001
Default mode	<0.01	0.32	0.31	0.28	0.02	0.07	3765	
Total vertices	1218	6400	6805	2572	648	836		

1052
1053 [1]Kolmogorov-Smirnov tests for independence of samples were calculated between each network and the DMN.
1054
1055 *Note:* entries in the centre of the table are proportions, which are provided relative to the functional network (ie: 29% of the visual
1056 network is koniocortical), thereby the rows approximately sum to 1 (given rounding errors).
1057
1058 Kon=koniocortical. Eu=eulaminate. Dys=dysgranular. Ag=agranular. DAN=dorsal attention network. VAN=ventral attention
1059 network.
1060
1061

Supplementary Table 2: Correlation of DMN connectivity with cytoarchitectural axis

Measure of connectivity	Dataset	All non-DMN	Koniocortical	Eulaminate-III	Eulaminate-II	Eulaminate-I	Dysgranular	Agranular
E_{NAV} (Structural model)	MICS	**r=-0.60, p<0.001**	**r=-0.64, p<0.001**	**r=-0.60, p<0.001**	**r=-0.37, p=0.006**	r=-0.29, p=0.066	r=0.08, p=0.672	r=0.17, p=0.847
	HCP	**r=-0.37, p<0.001**	**r=-0.45, p<0.001**	**r=-0.64, p<0.001**	r=-0.23, p=0.145	r=-0.16, p=0.198	r=0.06, p=0.380	r=0.30, p=0.080
Input (Functional model)	MICS	**r=-0.41, p<0.001**	**r=-0.36, p<0.001**	**r=-0.45, p<0.001**	**r=-0.21, p<0.001**	**r=-0.44, p<0.001**	r=-0.23, p=0.014	**r=-0.37, p<0.001**
	HCP	**r=-0.40, p<0.001**	r=-0.23, p=0.020	**r=-0.49, p<0.001**	**r=-0.31, p<0.001**	r=-0.18, p=0.063	r=-0.20, p=0.091	**r=-0.20, p=0.019**
Output (Functional model)	MICS	r=-0.18, p=0.069	r=-0.09, p=0.302	r=-0.22, p=0.026	r=0.13, p=0.025	r=0.07, p=0.424	r=-0.15, p=0.284	r=-0.04, p=0.411
	HCP	**r=-0.31, p=0.004**	**r=-0.33, p=0.003**	**r=-0.41, p<0.001**	r=-0.19, p=0.016	r=-0.26, p=0.032	r=-0.14, p=0.396	r=-0.29, p=0.012
Input (Extended functional model)	MICS	**r=-0.45, p<0.001**	**r=-0.42, p<0.001**	**r=-0.54, p<0.001**	**r=-0.22, p<0.001**	**r=-0.41, p<0.001**	r=-0.23, p=0.086	r=-0.23, p=0.061
	HCP	**r=-0.39, p<0.001**	**r=-0.28, p=0.004**	**r=-0.47, p<0.001**	r=-0.29, p=0.011	r=-0.20, p=0.007	r=-0.12, p=0.310	r=-0.13, p=0.180
Output (Extended functional model)	MICS	r=-0.12, p=0.200	r=-0.18, p=0.131	r=-0.02, p=0.035	r=0.02, p=0.220	r=-0.23, p=0.725	r=0.04, p=0.058	r=0.15, p=0.857
	HCP	**r=-0.36, p<0.001**	**r=-0.32, p=0.001**	**r=-0.43, p<0.001**	r=-0.23, p=0.033	**r=-0.21, p=0.004**	r=-0.12, p=0.240	r=-0.19, p=0.061

Note: p-values reflect a two-sided comparison with 10,000 permutations. Significance (in bold) was deemed where p<0.004, which reflects a Bonferroni correction for seven two-side tests (each row of the table), with an alpha level of 0.05.

Supplementary Table 3: Imbalance of connectivity across cortical types

Measure of connectivity	Dataset	Visual	Somato-motor	Dorsal attention	Ventral attention	Limbic	Fronto-parietal	Default mode
E_{NAV} (Structural model)	MICS	KL=0.069, p=0.827	KL=0.011, p=0.117	KL=0.026, p=0.879	KL=0.006, p=0.132	KL=0.063, p>0.999	KL=0.007, p=0.037	KL=0.001, p=0.176
	HCP	KL=0.091, p=0.389	KL=0.032, p=0.144	KL=0.082, p=0.949	KL=0.027, p=0.352	KL=0.086, p>0.999	KL=0.028, p=0.036	KL=0.007, p=0.201
Input (Functional model)	MICS	KL=0.003, p=0.033	KL=0.024, p=0.660	KL=0.021, p=0.828	KL=0.032, p>0.999	KL=0.048, p>0.999	KL=0.025, p=0.477	KL=0.048, p=0.910
	HCP	KL=0.033, p=0.411	KL=0.032, p=0.809	KL=0.017, p=0.548	KL=0.092, p>0.999	KL=0.019, p=0.677	KL=0.039, p=0.822	KL=0.022, p=0.827
Output (Functional model)	MICS	KL=0.012, p=0.224	KL=0.062, p=0.987	KL=0.050, p>0.999	KL=0.106, p>0.999	KL=0.014, p=0.108	KL=0.040, p=0.761	**KL=0.003, p=0.001**
	HCP	KL=0.043, p=0.326	KL=0.131, p>0.999	KL=0.056, p=0.861	KL=0.096, p>0.999	KL=0.018, p=0.128	KL=0.031, p=0.423	**KL=0.004, p<0.001**
Input (Extended functional model)	MICS	KL=0.013, p=0.221	KL=0.017, p=0.695	KL=0.004, p=0.999	KL=0.064, p>0.999	KL=0.040, p=0.924	KL=0.029, p>0.999	KL=0.013, p=0.841
	HCP	KL=0.111, p=0.869	KL=0.092, p=0.695	KL=0.116, p=0.978	KL=0.194, p>0.999	KL=0.036, p=0.052	KL=0.091, p=0.834	KL=0.045, p=0.001
Output (Extended functional model)	MICS	KL=0.040, p=0.513	KL=0.051, p=0.887	KL=0.085, p>0.999	KL=0.108, p>0.999	KL=0.022, p=0.209	KL=0.061, p>0.999	**KL=0.008, p<0.001**
	HCP	KL=0.056, p=0.337	KL=0.158, p>0.999	KL=0.117, p=0.978	KL=0.150, p>0.999	KL=0.029, p=0.078	KL=0.073, p=0.612	**KL=0.032, p<0.001**

Note: p-values reflect a one-sided comparison with 10,000 permutations. Significance (in bold) was deemed where p<0.007, which reflects a Bonferroni correction for seven one-side tests (tests within a row of the table), with an alpha level of 0.05.